FIRST-PRINCIPLES STUDIES OF THE LOW DIMENSIONAL TRANSITION METAL OXIDES

by

JIAO AN

DISSERTATION

Submitted in partial fulfillment of the requirements

for the degree of Doctor of Philosophy at

The University of Texas at Arlington

August, 2019

Arlington, Texas

Supervising Committee:

Qiming Zhang, Supervising Professor

Muhammad Huda

J. Ping Liu

Joseph Ngai

Alex Weiss

ABSTRACT

FIRST-PRINCIPLES STUDIES OF THE LOW DIMENSIONAL TRANSITION METAL OXIDES

Jiao An, Ph. D.

The University of Texas at Arlington, 2019

Supervising Professor: Qiming Zhang

Transition metal oxides have drawn lots of attention from experimental and theoretical research due to their unique physical and chemical properties. Among them, the semiconducting α-Fe_2O_3 and TiO_2 has been investigated for their potential use in a wide range of applications, such as photocatalysis, electrochemistry, and solar cells.

Hematite α-Fe_2O_3 is a potential low-cost, earth-abundant, and environment-friendly semiconducting material. It was found that the isovalent sulfur-doping could reduce its band gap. To study the interaction of a sulfur atom with the surface of α-Fe_2O_3, a model of α-Fe_2O_3 (0001) film is made. From the optimized bulk structure, the clean hematite α-Fe_2O_3 (0001) film is built of 12 atomic layers with two different types of termination. And the most stable film is terminated by Fe atoms with an anti-ferromagnetic arrangement. For a sulfur atom adsorption on the suface of this film, the results suggest that the sulfur atom prefers to stay at the surface. There is a high barrier about 2 eV for the sulfur atom penetrating into the film. This excludes the possibility of tuning the band gap of α-Fe_2O_3 through the sulfurization of the oxide surfaces.

The geometric and electronic properties of the TiO_2 single-walled and double-walled nanotubes have been investigated. The stabilities of the nanotubes have been studied. For the single-wall nanotube (SWNT), the strain energy is decreased with the increase of the radius of the nanotube. The band gap energy is increased with the increase of the radius, approaching to the band gap energy of the HexABC sheet (~3.54 eV). Especially, the band gap of the (6,0) SWNT is reduced to about 2.86 eV, due to its reconstruction. The isovalent sulfur atom (S) doping with nanotubes has also been studied. The band gap values of double-wall nanotubes (DWNT) are decreased significantly compared with that of single-wall nanotubes due to the offset of the bands of the two constitutive single-wall nanotubes. It shows that the TiO_2 DWNTs with smaller innershell radii form a type II band alignment, the staggered gap. And the band gap of the NTs studied could cover the redox potentials of water splitting, by comparing the band gap position of the bulk anatase with respect to the redox potentials of water splitting.

ACKNOWLEDGEMENTS

Upon the completion of this thesis, I would like to thank my respectable supervisor Dr. Qiming Zhang, who provided his great guidance, advice, and support for me to complete this dissertation. Dr. Zhang, as my supervising professor, encouraged me to think independently and helped me during the research of my studies. For each published paper, we work together and he had been patient to give so many instructions for my work. And he also gives me constructive suggestions, which are beneficial to me a lot, for my studies in my Ph. D program. When I just came to the University of Texas at Arlington, Dr. Zhang also gave me great help.

Next, my sincere gratefulness and particular thanks moves to my committee members, Dr. M. Huda, Dr. P. Liu, Dr. J. Ngai, and Dr. A. Weiss. They take their valuable time to participate in my oral comprehensive exam and also my dissertation defense exam. I would like to thank Dr. Prabath Wanaguru for his help in my research and life at UTA. I would like to also express my gratitude to the Physics Department for supporting my time here at UTA. I would like to acknowledge my fellow group members Yuting Peng, Zhi Tan, and Xu Zhao for their support.

Finally, I would like to recognize my mother and father for their support throughout my Ph. D. program. They always give me the love and support what they have totally. Their love is always the source of my strength. Thanks for the help and support of Dr. Chuanlong Lin. Thanks to all the people who helped me during my studies in UTA.

July, 2019

TABLE OF CONTENTS

LIST OF FIGURES

LIST OF TABLES

Chapter 1

Introduction

With a rapid development of the world economy, the global energy consumption keeps increasing. And from the latest international energy outlook 2017 (IEO2017) [1], it shows that the world energy consumption will grow by 28% between 2015 and 2040. As shown in Fig. 1.1, through 2040, world consumption of marketed energy is increased from all fuel sources, except for coal demand, which is kept essentially flat. Among these sources, renewable energy sources will be the fastest-growing energy source as expected, with consumption increasing by an average 2.3% per year between 2015 and 2040. Half of the growth in global energy demand comes from the power sector, in response to higher electricity consumption. And it is shown in Fig. 1.1 that the solar PV and wind generate only 7% of the electricity in 2018. Solar energy can also be collected and stored directly, which could be the heat provider for people. It is well known that the fossil fuels, which include coal, oil, and natural gas, have the advantages of high density, lower cost, and convenience. But they also have some disadvantages, such as limited deposits, pollution and causing green house gases effect. For the renewable energy, the advantages are exhaustless and environment-friendly, even though some of them has high cost and low efficiency. So considering the huge energy demand and the current percentage contributed by solar energy harvest, there is still a large room to catch up for the transfer of solar energy to electricity.

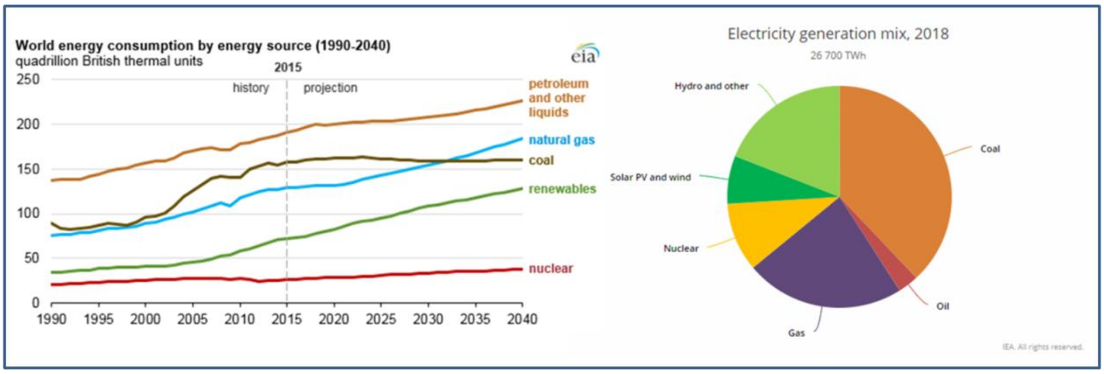

Source from IEA

Figure 1.1. The word energy consumption (the left side) and electricity generation mix in 2018 (the right side) from IEA.

Photovoltaic (PV) cells and photocatalysis are most popular categories for converting the energy of sunlight to other types of energies used in our life. PV cells are also called solar cells. It is made by one or multiple semiconductor p-n junction shown in Fig. 1.2. The p-n junction is formed by a p-type and n-type semiconductor aligned by the Fermi level. If the energy of the photon is smaller than the band gap value of the material, there will be no light absorption. If the energy of the photon is equal to or larger than the band gap value of the material, there will be light absorbed and one electron will be excited to the conduction band from the valence band, leaving a hole in the valence band. The electron-hole pair is then separated by the p-n junction. The electrons prefer to stay in n-type region, and the holes prefer to stay in p-type site. The process is equivalent to an e.m.f. or battery. The ideal semiconductor materials for the p-n junction would cover almost all of solar visible frequencies and some infrared spectra. The optimal band gap energy of the semiconductor material is calculated as about 1.4 eV by Shockley-Queisser model. One familiar semiconductor is silicon, with a band gap of 1.1 eV. The efficiency of the single-crystalline Si is reported as 25.6%, while the efficiency of the poly-crystalline Si is about 20.8%.

Single-crystalline Si cell has reached the almost complete light trapping and carrier collection, but the limit is the carrier recombination. Today the PV market is dominated by the crystalline Si solar modules with the market share of 90%.

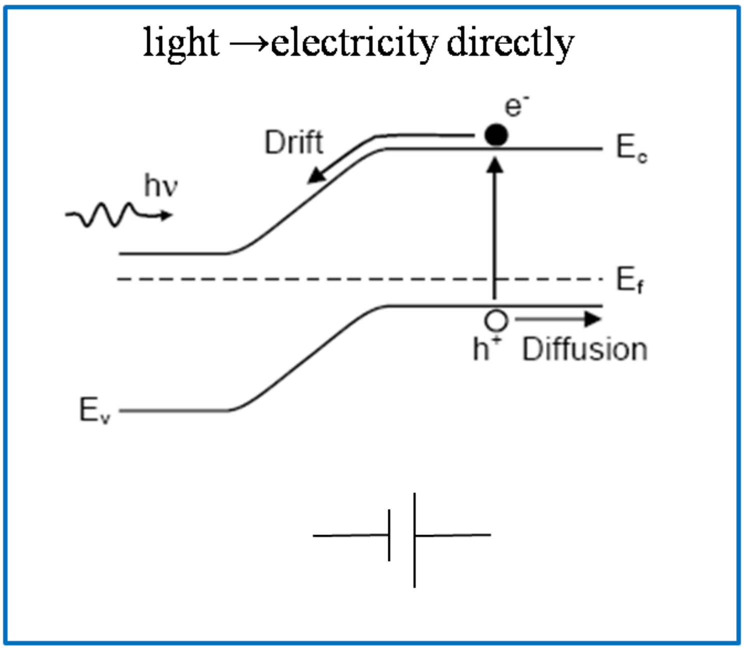

Figure 1.2. The working principles of solar cells.

So far, there are also some other materials, CdTe, GeAs, perovskite materials, CIGS, nano crystals, and so on. Most of them are still in the research stages [2]. The efficiency of a laboratory CdTe solar cell is 22.1%, but the element Cd is not environment-friendly. For the thin film of GaAs, incomplete light trapping and absorption in the metal result in some current loss. And because of the toxic element As, it should be careful about the recycling of commercial GaAs modules. As a represent of III-V compound, InP, has similar band gap value with GaAs, but the efficiency is lower than that of GaAs due to its lower voltage and lower current. And the material Indium is also high cost one, due to the limited deposit on earth. The efficiency of $Cu(In,Ga)(SeS)_2$ (CIGS), as recorded, has steadily increased at 21.7%. The indium is a key element to these materials. The record published efficiency for quantum dot (QD) solar cells is 9.9% using PbS QDs with band gap energy of 1.4 eV. But this cell has very large voltage loss. And there is current loss due to light reflection and incomplete light trapping.

The semiconducting materials for the massive applications of PV cells should have some good key qualities, such as the cost-effective, earth-abounded and environment-friendly. Some semiconducting transition metal oxides, such as copper oxides, iron oxides, satisfy these requirements. But their band gaps are higher. Therefore, to find semiconductor materials with these qualities and to engineer their band gap values to improve the efficiency of these materials are two popular researching topics in the solar-cell materials research.

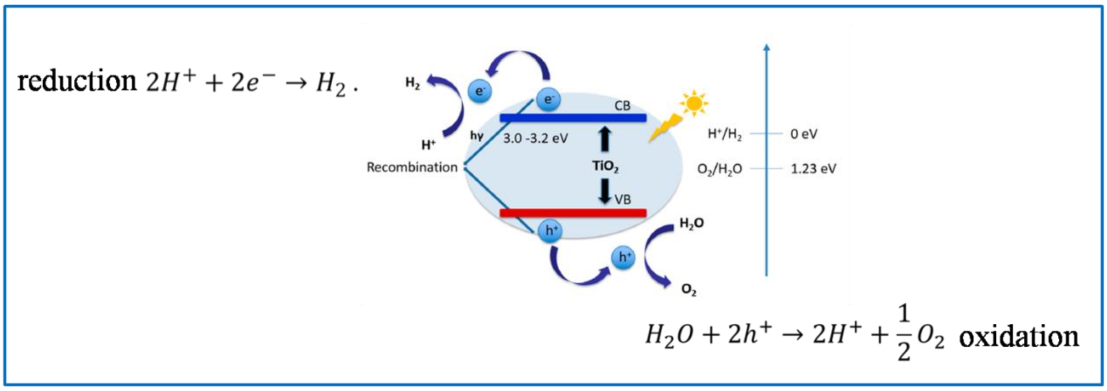

Figure 1.3. The working principles of photocatalysis. Figure is from reference [74].

Another extensive-studied branch of converting solar energy is photocatalysis. Photocatalytic activity is to generate the hydrogen gas from water splitting reaction by absorbing solar energy. Fujishima and Honda first achieved an electrochemical photocatalysis of water by TiO_2 in 1972 [3]. TiO_2 is suitable for photocatalysis due to its common availability, relatively low cost, and high chemical stability. To be photocatalytic material, the work principle of photocatalysis shown in Fig. 1.3 requires certain characters. The reaction of photocatalytic water-splitting is initiated by photon absorption. This means the photo energy will be larger than the band gap energy. And then it will generate numerous electron-hole pairs with sufficient potentials. The electron will reduce water to generate the hydrogen gas, and the hole will oxidize water to generate oxygen gas. So the minimum band gap for one suitable water splitting photocatalyst should be 1.23 eV. But for the most candidates of the photocatalytic materials, they work under ultraviolet light, which just occupies only 4% of total solar light. To improve the efficiency of the photocatalyst, engineering semiconductors for band gap energy to the visible light range is a research direction. The other major challenge is the recombination of electrons and holes. For example, surface defect usually serves as adsorption site for the recombination of electrons and holes, thus decreasing the efficiency of the photocatalytic reaction. And the modification of the efficiency of photocatalytic activities of TiO_2 has been studied experimentally and theoretically [4]. With development of nanoscience and nanotechnology, the nanostructures of TiO_2 have drawn a lot of attentions from different research groups [5, 6]. Therefore, engineering the band gap of semiconductor materials for PV cells and photocatalysis will be one of most meaningful theoretical studies, and will give us a better understanding of the electronic properties of materials. That is the focus of this dissertation.

Density functional theory (DFT) is a computational quantum mechanical modeling method to investigate the electronic properties of the multi-body systems. And it has already been one of the most popular tools for condensed matter physics, computational physics and computational chemistry. In this dissertation, a brief review of DFT and its implementation in computational package are present in Chapter 2. Chapter 3 presents the studies of the electronic properties the pure film of $\alpha\text{-}Fe_2O_3$ and with the sulfur atom doping. Chapter 4 shows the studies of the single walled nanotubes of TiO_2 with armchair and zigzag chiralities and with the sulfur atom doping. Chapter 5 reports the studies of the double walled nanotubes of TiO_2 with these two chiralities. A conclusion is given in Chapter 6.

Chapter 2

Methodology

The systems interested in materials science consist of tremendous number of particles, including nuclei and electrons. The right theory to describe them is quantum mechanics. However, in the actual application, it is found that there is few system that can be solved analytically. Even though the simplest hydrogen atom can be solved, it is impossible to study a more complex condensed matter system. So there are some approximate methods are needed to apply in quantum mechanics.

Density functional theory is a method of obtaining an approximate solution to the Schrödinger equation of a many-body system. And now it is one of the most useful theories in the last two decades to study the properties of the condensed matter systems. In the following section, density functional theory will be discussed briefly.

2.1 The approximate methods in Quantum mechanics

The basic problem in quantum mechanics is how to describe the state of the system, *ie* solving the wave function and the energy of the system that it may have. However, the different systems will be treated with the different Schrödinger equations. And sometimes the Hamiltonian of the system is too complicated to solve. At this time, the exact solution cannot be given. The approximate solution can only be obtained by using some approximation. Therefore, it is very important to use the approximation methods to solve physical problems in quantum mechanics.

2.1.1 Born-Oppenheimer approximation

Without considering the external field, the Hamiltonian of a multi-particle system in condensed matter physics should include the kinetic energy of the nuclei and electrons and the interaction energy between these particles,

$$\hat{H} = -\frac{1}{2}\sum_{i=1}^{N}\nabla_i^{\,2} - \frac{1}{2}\sum_{A=1}^{M}\frac{1}{M_A}\nabla_A^{\,2} - \sum_{i=1}^{N}\sum_{A=1}^{M}\frac{Z_A}{r_{iA}} + \sum_{i=1}^{N}\sum_{j>i}^{N}\frac{1}{r_{ij}} + \sum_{A=1}^{M}\sum_{B>A}^{M}\frac{Z_A Z_B}{R_{AB}} ,$$

(2-1)

where the first term is the kinetic energy of the electrons, the second term is the kinetic energy of the nuclei, the third term is the electron-nuclei interaction, the forth term is the coulomb interaction energy between all the electrons, the last term is the coulomb interaction energy between all the nuclei. And to simplify the equations, the atomic unit $(e = 1, \hbar = 1, m_e = 1, 4\pi\varepsilon_0 = 1)$ is used here.

The third term is not only a function of the electronic coordinates, but also is a function of nuclear coordinates. And it has the same order of magnitude as other interaction terms, so it cannot be simply ignored. Since the mass of a nucleus is about three orders of magnitude larger than the electron mass, according to the conservation of momentum, the velocity of the nucleus is much smaller than that of the electron. When electrons are moving at high speeds, the nuclei can only follow the changes of electrons slowly. Born and Oppenheimer proposed that the whole problem can be divided into the two parts: the motion of electrons and the motion of the nuclei. It means that the nucleus is in its instantaneous position when considering electron motion, but the space distribution of the electrons is not considered when considering the motion of the nuclei. This is called Born-Oppenheimer approximation [7], or the adiabatic approximation.

The Schrödinger equation for multi-particle systems is

$$\hat{H}\psi(\vec{r},\vec{R}) = E^H \psi(\vec{r},\vec{R}), \tag{2-2}$$

where $\vec{r}$ is the coordinates of all the electrons, and $\vec{R}$ is the coordinates of all the nuclei. In the case of adiabatic approximation, the solution is separated as

$$\psi(\vec{r},\vec{R}) = \chi(\vec{R})\phi(\vec{r},\vec{R}), \tag{2-3}$$

where $\chi(\vec{R})$ is the wave function of all the nuclei in the system, and $\phi(\vec{r},\vec{R})$ is the wave function of all the electrons in the system. The wave function of electrons $\phi(\vec{r},\vec{R})$ is the solution of the Schrödinger equation corresponding to the Hamiltonian operator of the electron part for the system shown below,

$$\hat{H}_0 = -\frac{1}{2}\sum_{i=1}^{N}\nabla_i^2 - \sum_{i=1}^{N}\sum_{A=1}^{M}\frac{Z_A}{r_{iA}} + \sum_{i=1}^{N}\sum_{j>i}^{N}\frac{1}{r_{ij}}, \tag{2-4}$$

$$\hat{H}_0(\vec{r},\vec{R})\phi(\vec{r},\vec{R}) = E(\vec{R})\phi(\vec{r},\vec{R}). \tag{2-5}$$

The instantaneous position coordinates of the nuclei ($\vec{R}$) are set as the parameters in the electron wave functions.

2.1.2 Variational principle

The condition for dealing with the quantum mechanical problems with perturbation theory is that the Hamiltonian of the representative system can be divided into two parts, the non-perturbation term can be solved or the solution is known, and the part of the perturbation term is tiny. If these two conditions cannot be met, perturbation theory cannot be applied. Then another approximation method could be considered, the variation principle.

The basic idea of applying the variation principle to the quantum problem is to select a type of testing wave function with respect to the specific problem, to give the average energy $\bar{E}$

corresponding to the testing wave function, and then to take the minimum value of $\bar{E}$ to find the best wave function and the corresponding average energy, which are used as the exact approximation solution of the eigenfunction and energy eigenvalues of the system. Here, the Hartree-Fock method, as an example of variational methods, is introduced briefly.

By the Born-Oppenheimer approximation, the electronic motion can be successfully separated from the nucleus motion in a multi-particle system. When considering the motion of electrons, the nuclei can be fixed, and the electrons move in the potential field formed by all the nuclei. When the relative position of the nucleus is changed, the state of the electron motion will also change. So the repulsive interaction between the nuclei must be added to the energy of the electronic system. The repulsive potential between the nuclei $\hat{V}_{N-N}(\vec{R})$ is only related to the position between the nuclei. For those systems which the positions of the nuclei are determined, $\hat{V}_{N-N}(\vec{R})$ is a constant, and it can only affect the total energy of the electronic system, but not the wave function. So when solving the wave function of electrons, we do not need to add the repulsion energy between the nuclei, and finally add the repulsion item to calculate the electron energy. Then the Schrödinger equation of the electron part from equation (2-5) can be obtained,

$$\left[-\frac{1}{2}\sum_{i=1}^{N}\nabla_i^2-\sum_{i=1}^{N}\sum_{A=1}^{M}\frac{Z_A}{r_{iA}}+\sum_{i=1}^{N}\sum_{j>i}^{N}\frac{1}{r_{ij}}\right]\phi=\left[\sum_{i}\hat{H}_i+\sum_{i,j}{}'H_{ij}\right]\phi=E\phi\,, \quad (2\text{-}6)$$

where *i* or *j* is the index for electrons.

There are the coupling terms of different electrons from the above equation. So it is difficult to solve the exact solution, and it is no longer possible to solve the Schrödinger equation to obtain an approximate solution by the above method. So Hartree proposed that the product of the single electron wave functions φ_i (r_i) as an approximate solution of the Schrödinger equation for the multi-electron system,

$$\phi(r) = \varphi_1(r_1)\varphi_2(r_2)\cdots\varphi_i(r_i)\cdots\varphi_n(r_n) . \tag{2-7}$$

This approximation is called the Hartree approximation [8]. The wave function corresponding to (2-7) is called the Hartree wave function. The constructed many-body wavefunction (2-7) could be used as a trial solution to calculate the expectation value of the energy,

$$E[\phi] = \left\langle \phi \middle| \hat{H} \middle| \phi \right\rangle = \left\langle \hat{H} \right\rangle . \tag{2-8}$$

The variational principle states that the energy computed from the guess is an upper bound to the true ground-state energy E_0. If we minimize $\left\langle \hat{H} \right\rangle$ with respect to variation of φ_{i}^*, we obtain

$$\delta\left[\left\langle \hat{H} \right\rangle - \sum_{i=1}^{N} \varepsilon_i (\left\langle \varphi_j \middle| \varphi_i \right\rangle)\right] = 0 , \tag{2-9}$$

where φ_{i}^* satisfies the normalization equation $\left\langle \varphi_j \middle| \varphi_i \right\rangle = \delta_{ij}$, and ε_i is Lagrangian multiplier. The normalization condition acts as a constraint on the variation of $\left\langle \hat{H} \right\rangle$. As well known, the electron is a fermion since its spin quantum number is 1/2. But Hartree does not consider an exchange anti-symmetry of the electron wave function. For the system with N electrons with the position vectors $\vec{r}_1, \vec{r}_2, ..., \vec{r}_n$ the corresponding approximate wave functions can be expressed as the follow, the Slater determinant,

$$\phi(r) = \frac{1}{\sqrt{N!}} \begin{vmatrix} \varphi_1(\vec{q}_1) & \varphi_2(\vec{q}_1) & \cdots & \varphi_N(\vec{q}_1) \\ \varphi_1(\vec{q}_2) & \varphi_2(\vec{q}_2) & \cdots & \varphi_N(\vec{q}_2) \\ \cdots & \cdots & \cdots & \cdots \\ \varphi_1(\vec{q}_N) & \varphi_2(\vec{q}_N) & \cdots & \varphi_N(\vec{q}_N) \end{vmatrix} , \tag{2-10}$$

where $\varphi_i(\vec{q}_i)$ represents the normalized wave function of the *i*-th electron at the coordinate $\vec{q}_i$, including $\vec{r}_i$ and spin.

Using the Slater determinant, the expectation of the energy of the system is equal to the average value of the Hamiltonian of the system acting on the above determinant. In the other words, by the variation principle, the wave function φ constructed by the best single electron wave function φ_i could give the minimum value of the system energy E. Then do the variation on E with respect to the φ_i and use ε_i as the Lagrange multiplier to get the one-electron wave function to satisfy the following differential equation,

$$\left[-\frac{1}{2}\nabla^2+V(r)\right]\varphi_i(r)+\sum_{j(\neq i)}\int dr'\frac{\left|\varphi_j(r')\right|^2}{\left|r-r'\right|}\varphi_i(r)-\sum_{j(\neq i)}\int dr'\frac{\varphi^*{}_j(r')\varphi_i(r')}{\left|r-r'\right|}\varphi_j(r)=\varepsilon_i\varphi_i(r), \tag{2-11}$$

where $V(r)$ is the potential between the nuclei and electrons.

Equation (2-11) is called as the Hartree-Fock equation.

The charge distribution is defined as

$$\rho(r')=\sum_i\rho_i(r')=\sum_i\left|\varphi_i(r')\right|^2. \tag{2-12}$$

And the exchange charge distribution is defined as

$$\rho_i^{HF}(r,r')=\sum_{j(\neq i)}\frac{\varphi_j^*(r')\varphi_i(r')\varphi_i^*(r)\varphi_j(r)}{\varphi_i^*(r)\varphi_i(r)}. \tag{2-13}$$

Plug (2-12) and (2-13) into (2-11), and the Hartree-Fock equation can be written as

$$\left[-\frac{1}{2}\nabla^2+V(r)+\int dr'\frac{\rho(r')-\rho_i^{HF}(r,r')}{\left|r-r'\right|}\right]\varphi_i(r)=\varepsilon_i\varphi_i(r). \tag{2-14}$$

The Hartree-Fock equation can only be solved by the iterative method. Firstly, the solution of the Hartree-Fock equation is a set of single-electron states $\{\varphi_i\}$. The potential function is obtained from the set single-electron states, and the equation could be solved to get a better solution {φ_i}. This process is repeated until that {φ_i} is no longer changed within the calculation accuracy considered. This is called as the Hartree-Fock self-consistent field approximation method [8, 9]. And the Eq. (2-14) can be further simplified as

$$\left[-\frac{1}{2}\nabla^2 + V_{eff}(r)\right]\varphi_i(r) = \varepsilon_i\varphi_i(r), \tag{2-15}$$

where

$$V_{eff}(r) = V(r) + \int dr' \frac{\rho(r') - \bar{\rho}^{HF}(r,r')}{|r-r'|}, \tag{2-16}$$

$$\rho_i^{HF} = \bar{\rho}^{HF} = \sum_i \frac{\varphi_i^*(r)\varphi_i(r)\bar{\rho}_i^{HF}(r,r')}{\sum_i \varphi_i^*(r)\varphi_i(r)} \ . \tag{2-17}$$

Then Eq. (2-14) is written as a one-electron effective potential equation. Since the total wave function of the electrons satisfies the exchange anti-symmetry, the interaction of the electrons which have the same spin and the same position is canceled, so that it is impossible to simultaneously have the electrons with the same spin at the same position. But at the same time, due to the existence of Coulomb repulsion, it cannot allow the electrons with the opposite spins to appear at the same position. The energy corresponding to this term is called the correlation term, which is the missing part of the Hartree-Fock approximation.

2.2 Density Functional Theory

The systems we encounter in solving practical problems are more multi-particle systems, such as molecules, solids, or systems with large numbers of particles. The approximation and simplification can be done by using the methods described above. However, density functional theory for solving the single-electron problems is a more rigorous and precise theory. It not only provides a theoretical basis for transforming the multi-electron problems into the easily solved single-electron problems, but also becomes an effective theoretical tool for computing the total energy and the electronic structure for the multi-particle systems.

2.2.1 Hohenberg-Kohn theorem

Density functional theory originated from the work of H. Thomas and E. Fermi in 1927 [10, 11]. The main idea is that the physical properties of the ground state of molecules and solids can be represented by the density of the particles. The basis of density functional theory is the theory of non-uniform electron gas proposed by P. Hohenberg and W. Kohn [12]. This theory can be summarized as the following two parts. First, without considering the spin, for the identical fermions system, its energy of the ground state is the only functional of the particle number density function $\rho(r)$. Second, in the case where the number of the particles does not change, the energy functional $E[\rho]$ has a minimum value of the particle number density function $\rho(r)$ and this minimum value would be equal to the energy of the ground state.

They are called Hohenberg-Kohn theorem. The first part shows that all the physical properties of the ground state of the multi-particle system are uniquely determined by the particle number density function. The second part shows that as long as the ground state of the particle density function is obtained, the minimum value of the energy functional can be obtained, and this minimum value is equal to the ground state energy of the corresponding system. Therefore, the minimization of energy functional with respect to the particle number density is a method to determine the ground state of the system.

According to the above, we can write the energy functional of the multi-electron system with respect to the electron number density, which has the corresponding electron kinetic energy and the interaction between the electron, the role of the external field, *e.g.* nuclei, and the interaction between the nuclei in the Hamiltonian, respectively.

$$E\left[\rho\right]=F\left[\rho\right]+E_{ext}\left[\rho\right]+E_{N-N}, \tag{2-18}$$

where $F\left[\rho\right]=T\left[\rho\right]+\frac{1}{2}\iint drdr'\frac{\rho(r)\rho(r')}{\left|r-r'\right|}+E_{XC}\left[\rho\right]$ contains the kinetic energy of the electrons and the interaction energy between the electrons. $E_{XC}\left[\rho\right]$ represents the non-included interaction energy of the all non-interacting particle models, which is called the exchange correlation energy.

2.2.2 Kohn-Sham equation

To determine electron density and the kinetic energy functional, W. Kohn and L. J. Sham [13] proposed that if the kinetic energy functional of the system studied can be replaced by a kinetic energy functional of a known non-interacting electronic system, and the density functions of the two systems are the same, and this density function can be composed of the number of N single electron wave functions,

$$\rho(r)=\sum_{i=1}^{N}\left|\varphi_i(r)\right|^2. \tag{2-19}$$

It can be obtained that

$$T\left[\rho\right]=T_s\left[\rho\right]=\sum_{i=1}^{N}\int dr\varphi_i^*(r)(-\nabla^2)\varphi_i(r). \tag{2-20}$$

Then the variation of the energy functional to the density function $\rho(r)$ is substituted for the variation on the wave function $\varphi_i(r)$. And then the variation with restrain of orthonormal conditions is obtained as

$$\left\{-\frac{1}{2}\nabla^2+V_{KS}[\rho(r)]\right\}\varphi_i(r)=\varepsilon_i\varphi_i(r), \tag{2-21}$$

where

$$\begin{aligned} V_{KS}[\rho(r)] &= v(r) + V_{coul}[\rho(r)] + V_{XC}\left[\rho(r)\right] \\ &= v(r) + \int dr' \frac{\rho(r')}{|r-r'|} + \frac{\delta E_{XC}\left[\rho(r)\right]}{\delta\rho(r)} . \end{aligned} \qquad (2\text{-}22)$$

Equation (2-21) is a single-electron equation similar to the Hartree-Fock equation (2-11). Corresponding to the effective potential of the Hartree-Fock equation, $V_{KS}[\rho(r)]$ includes Coulomb repulsive potential, exchange-related potential, and external field potential . We refer to the three equations (2-19), (2-21), and (2-22) as the Kohn-Sham equations.

The center of the Kohn-Sham equation is to replace the kinetic energy of the electronic system with interaction by the kinetic energy of the electron system without interaction, and to attribute the full complexity of the interacting electronic system to the functional of the exchange-correlation potential. So a simple one-electron equation is obtained as the Eq. (2-21). Comparing with the Hartree-Fock equation, the Kohn-Sham equation includes not only the exchange interaction of electrons, but also the correlation interaction of electrons. Therefore, the single-electron Kohn-Sham equation given by density functional theory (DFT) is rigorous.

2.3 Approach to solve a Kohn-Sham equation

2.3.1 Bloch theorem

Solid energy band theory is an important theory for studying the motion of electrons in the solids. It is also an approximation theory. The starting point is that the electrons in the solid do not belong to some single atom, but they move in the whole solid. These electrons are called the shared electrons. Bloch theorem [14] could solve the wave function of the so-called shared electrons moving in a periodic potential field.

Bloch's theorem: when the potential field $V(\vec{r})$ is a lattice periodic potential, the solution $\psi_n(\vec{r})$ of the wave equation,

$$H\psi_n(\vec{r}) = \left\{ -\frac{\hbar^2}{2m}\nabla^2 + V(\vec{r}) \right\} \psi_n(\vec{r}) = \varepsilon_n \psi_n(\vec{r}), \qquad (2\text{-}23)$$

has the following properties

$$\psi_n(\vec{k}, \vec{r} + \vec{R}_m) = e^{i\vec{k}\cdot\vec{R}_m} \psi_n(\vec{k}, \vec{r}), \qquad (2\text{-}24)$$

where $\vec{k}$ is the wave vector, and $\vec{R}_m$ is the lattice translation vector. Due to the periodic boundary condition, $\vec{k}$ is not continuous in the reciprocal space.

And $\vec{k} = \frac{l_1}{N_1}\vec{b}_1 + \frac{l_2}{N_2}\vec{b}_2 + \frac{l_3}{N_3}\vec{b}_3$ (2-25), where $\vec{b}_1$, $\vec{b}_2$, and $\vec{b}_3$ is the reciprocal lattice basis of the crystal, and N_1, N_2, and N_3 are the numbers of the primitive cell in the $\vec{a}_1$ $\vec{a}_2$, and $\vec{a}_3$ direction corresponding to the lattice base vectors. $\psi_n(\vec{k}, \vec{r})$ is called as the Bloch function. Here are some ways to calculate the energy bands.

2.3.2 Tight-binding approximation method

The focus of the tight-binding approximation method [15] is to use the linear combination of the atomic orbitals as a set of basis function for solving the single-electron Schrödinger equation. If the electron is near an atom, it would consider that the main potential is the nearest atomic potential, and the effect of other atoms on the electron is set as a perturbation.

The potential field in the crystal can be expressed as a linear superposition of the atomic potentials as follows,

$$V(\vec{r}) = \sum_l \sum_\alpha V^{at}(\vec{r} - \vec{R}_l - \vec{\tau}_\alpha), \qquad (2\text{-}26)$$

where $\vec{R}_l$ is the lattice translation vector and $\vec{\tau}_\alpha$ is the internal vector of the α-th atom of the l-th cell. The crystal Hamiltonian The wave function $\psi_n(\vec{k}, \vec{r})$ can be expressed as,

$$\psi_n(\vec{k},\vec{r}) = \sum_j A_{nj}\phi_j(\vec{k}\cdot\vec{r}), \tag{2-27}$$

where the basis $\phi_j(\vec{k}\cdot\vec{r})$ is a Bloch function consisting of the atomic orbit ϕ_j^{at}. Then

$$\phi_j(\vec{k}\cdot\vec{r}) = \frac{1}{\sqrt{N}}\sum_{l,\alpha} e^{i\vec{k}\cdot\vec{R}_l}\phi_j^{at}(\vec{r}-\vec{R}_l-\vec{\tau}_\alpha), \tag{2-28}$$

where $\phi_j^{at}(\vec{r}-\vec{R}_l-\vec{\tau}_\alpha)$ represents the *j*-th orbit of the *α*-th atom of the *l*-st cell, and *N* is the total number of the cells in the crystal.

Substituting the expression of the potential function (2-26) and the wave function (2-27) into the wave equation (2-23), and then multiplying by $\phi_{j'}(\vec{k}\cdot\vec{r})$ for both sides, we can obtain an equation about the linear combination coefficient $\{A_{nj}\}$,

$$\sum_j \left[H_{j'j} - \varepsilon_n(\vec{k})S_{j'j}\right]A_{nj} = 0, \tag{2-29}$$

where $H_{j'j} = \left\langle \phi_{j'} \middle| H \middle| \phi_j \right\rangle$, and $S_{j'j}$ is the overlap matrix, $S_{j'j} = \left\langle \phi_{j'} \middle| \phi_j \right\rangle$.

Similarly, if the coefficient $\{A_{nj}\}$ has a non-zero solution, then it must be satisfied,

$$\det\left|H_{j'j} - \varepsilon_n(\vec{k})S_{j'j}\right| = 0. \tag{2-30}$$

Solving generalized eigenvalue equations gives the function $\varepsilon_n(\vec{k})$ and A_{nj} 's.

2.3.3 Plane wave method

In the calculation methods of the crystal energy band, the plane wave method (PW) [16] is a simple method with the definite physical meaning, in which a linear combination of a series of plane waves $e^{i\vec{k}\cdot\vec{r}}$ with a difference by a reciprocal lattice vector is used to describe a Bloch function for the motion of electrons in a crystal.

Suppose that the potential function $V(\vec{r})$ have the lattice periodicity and expand it to the Fourier series as follows,

$$V(\vec{r}) = \sum_m V(\vec{G}_m)e^{i\vec{G}_m\cdot\vec{r}}, \tag{2-31}$$

where $\vec{G}_m$ represents the reciprocal lattice vector, and $V(\vec{G}_m)$ is the Fourier expansion coefficient,

$$V(\vec{G}_m)=\frac{1}{\Omega}\int drV(\vec{r})e^{-i\vec{G}_m\cdot\vec{r}}\ , \qquad (2\text{-}32)$$

where Ω is the volume of the primitive cell. Bloch function $\psi_n(\vec{k},\vec{r})=e^{i\vec{k}\cdot\vec{r}}u_n(\vec{k},\vec{r})$, where $u_n(\vec{k},\vec{r})$ is a function with the same period as the lattice, can also be expressed by the Fourier expansion,

$$\psi_n(\vec{k},\vec{r})=\frac{1}{\sqrt{N\Omega}}e^{i\vec{k}\cdot\vec{r}}\sum_m a(\vec{G}_m)e^{i\vec{G}_m\cdot\vec{r}}=\frac{1}{\sqrt{N\Omega}}\sum_m a(\vec{G}_m)e^{i(\vec{k}+\vec{G}_m)\cdot\vec{r}}\ , \qquad (2\text{-}33)$$

where *N* is the number of the primitive cells contained in the crystal. Substitute (2-27) and (2-29) into the wave equation, and multiply both sides by $e^{i(\vec{k}+\vec{G}_m)\cdot\vec{r}}$ to obtain that

$$\left[-\frac{\hbar^2}{2m}(\vec{k}+\vec{G}_n)^2-\varepsilon_n(\vec{k})\right]a(\vec{G}_n)+\sum_m V(\vec{G}_n-\vec{G}_m)a(\vec{G}_m)=0\,. \qquad (2\text{-}34)$$

Assuming that $\vec{G}_n$ has a different reciprocal lattice vector, we will get an equation set about the expansion coefficient. If $a(\vec{G}_m)$ had a non-zero solution, it must make the determinant of the equation set coefficient to zero, *i.e.*,

$$\det\left|\left[-\frac{\hbar^2}{2m}(\vec{k}+\vec{G}_n)^2-\varepsilon_n(\vec{k})\right]\delta_{G_nG_m}+V(\vec{G}_n-\vec{G}_m)\right|=0\,. \qquad (2\text{-}35)$$

The above equation is an infinite order determinant, and actually the computation takes a finite order of the determinant. Here, it should be stated that the nearly-free electron approximation method is a special case of the plane wave method. The common movement of the electrons in the crystal is very close to the motion of free electrons in the average potential field, and the difference between the real potential function and the average potential field is treated as perturbation. It will not be described in detail here. The advantage of the plane wave method is that the basis is independent of atomic coordinates. And the fruitful Fast Fourier Transformation (FFT) could be used. We can find that the disadvantage of the plane wave method is that a large number of plane waves are used to be combined into a Bloch function, so the amount of calculation will be quite large.

2.3.4 Pseudopotential Method

In the calculation of the energy band, the calculation for the full electron states is accurate, but the amount of the calculation is quite large and the convergence is very slow. In fact, the valence electrons are the most concerned part, because the state of valence electrons changes the most when forming the solid. The change of chemical environment has little effect on the inner electron wave function. Core electrons will be under the influence of a steep Coulomb potential and have rapidly varying wave functions in the nuclear regions. This requires a correspondingly large number of plane waves to adequately describe the wave function and the nuclear potential. This expense is reduced by the pseudopotential approximation.

Valence electrons are the electrons which are outside the core region and are responsible for the physical properties of a system for most situations. As the core electrons are unchanged in most situations, they could be replaced along with the nuclear potential, *i.e.* ions, to create a relatively weak pseudopotential. This pseudopotential acts on a set of pseudo wave functions that are identical to the wave functions outside of a specified core radius, where all the electrons are taken into account. The first step is to frozen core electrons with nuclei to be ions. For example, for one Ti atom, the electrons are $(1s)^2(2s)^2(2p)^6(3s)^2(3p)^6(4s)^2(3d)^2$. The core electrons $(1s)^2(2s)^2(2p)^6(3s)^2$ with the nucleus are the ion. The second step is to smooth the wave functions of valence electron $(3p)^6(4s)^2(3d)^2$. The pseudo wave functions have no nodes in the core region, and therefore it heavily reduces the number of plane waves required for the calculation. So the memory required for the calculation is also decreased. Because there are fewer Kohn-Sham orbitals required as the core electrons are not explicitly treated. An example of a pseudo wave function and pseudopotential compared to the all-electron counterparts are shown in Figure 3.

There are a number of methods popularly used to construct pseudopotentials. The two widely used methods are the norm-conserving approach and the ultrasoft approach. And they both show a good transferability for different condensed matter systems.

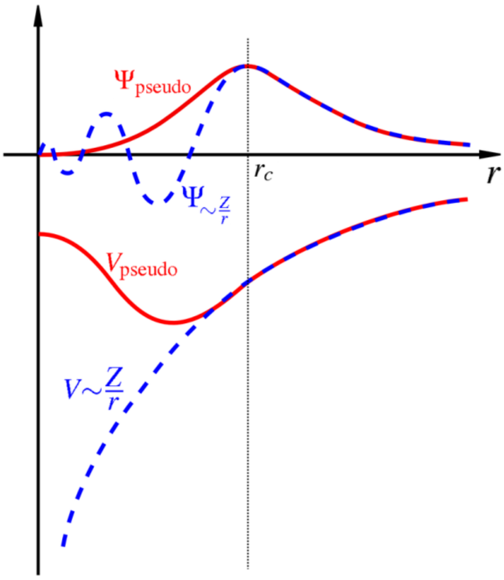

Figure 2.1 Comparision of a wave function in the Coulomb potential of the nucleus (blue) to the one in the pseudopotential (red). The real and the pseudo wave function and potentials match above a certain cutoff radius r_c. Figure is from Wikipedia.

2.3.5 Approximations for exchange-correlation term

Though DFT is rigorous, the exchange-correlation functional is unfortunately unknown. There are three popular approximations for exchange-correlation term $E_{XC}[\rho]$, which are shown briefly in the next.

(a) Local Density Approximation (LDA) [13, 17-18]

It is derived from homogenous electron gas and it approximates the energy functional of the real density by the energy function of a local constant density. Then exchange-correlation energy per particle of the system with density ρ ,

$$E_{XC}^{LDA}(\rho(\vec{r})) = \int \varepsilon_{XC}(\rho(\vec{r}))\rho(\vec{r})d\vec{r} \, . \qquad (2\text{-}36)$$

(b) Generalized Gradient Approximation (GGA) [12,19]

For GGA, the density changes with a rapid speed. So there is an improvement necessary for LDA. So the gradient of electron density is considered with GGA, and the exchange-correlation energy per particle of the system is shown as,

$$E_{XC}^{GGA}[\rho_{\uparrow}(\vec{r}), \rho_{\downarrow}(\vec{r})] = \int \varepsilon_{XC}\left(\rho_{\uparrow}(\vec{r}), \rho_{\downarrow}(\vec{r}), \vec{\nabla}\rho_{\uparrow}(\vec{r}), \vec{\nabla}\rho_{\downarrow}(\vec{r})\right)\rho(\vec{r})d\vec{r} \, . \qquad (2\text{-}37)$$

(c) Hybrid Functional(HSE06) [20, 21]

The functional uses a portion of the exact exchange term from Hartree–Fock theory and correlation from DFT, $E_{XC}^{Hyb} = \alpha E_{X}^{HF} + (1-\alpha)E_{XC}^{GGA}$. (2-38)

2.4 Computational Codes

The Vienna *ab initio* simulation package is currently one of the most popular commercial softwares in the material calculations. It was developed by the Hafner team at the University of Vienna and can be used for the calculations of the electronic structures and molecular dynamics simulations. VASP obtains the electronic state and energy of the system by solving the K-S equation iteratively. It can solve the Kohn-Sham equation on the basis of DFT and perform the calculations of hybrid density functional. VASP also supports the GW approach, the quasi-particle approximation [22] calculations, where G represents the Green's function of a single particle and W represents the screened Coulomb interaction. The plane wave basis set method and the interaction between electron and ion used in VASP are described by the method of the norm-conserving pseudopotentia (NCPP), the ultra-soft pseudopotential (USPP) [23] or alternatively the projected augmented wave (PAW) [24]. The flow chart of the VASP software package calculation is present below.

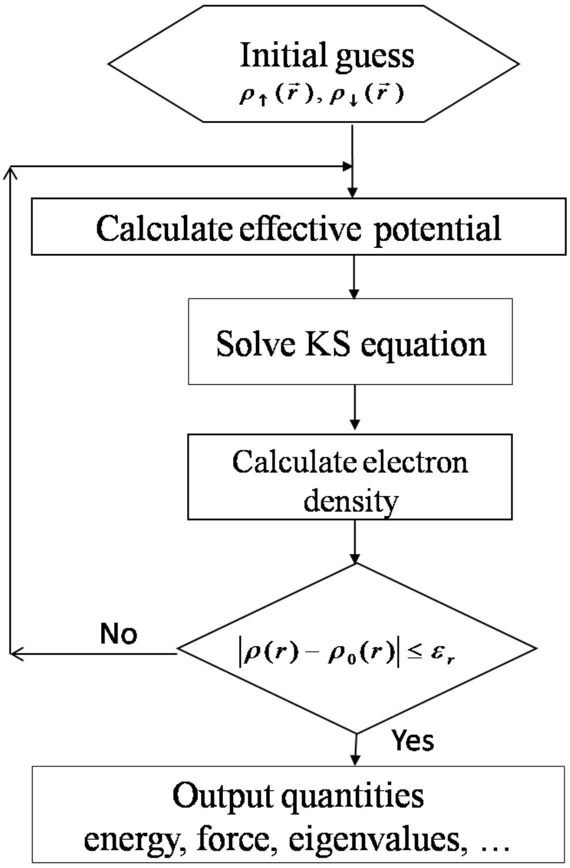

Chapter 3

Hematite α-Fe_2O_3 film and sulfur atom doping

3.1 Introduction

Transition metal oxides have drawn a lot of interest in both experimental and theoretical research due to their unique physical and chemical properties. As an important member of them, hematite α-Fe_2O_3 has been investigated for its potential use in a wide range of applications, such as catalysis, electrochemistry, magnetization, and environmental applications [25-28]. The various properties of the bulk and surface hematite have been studied extensively. It includes the studies on the crystal structures [29, 30], the electrical properties of the bulk [31] and its surface [32], and the magnetic properties [33, 34]. Moreover the optical properties of bulk and thin film α-Fe_2O_3 have been analyzed experimentally [35, 36].

Recently hematite α-Fe_2O_3 has drawn extensive interest due to its potential application in solar water splitting and solar energy conversion [37]. It is a cost-effective, earth-abundant and environment-friendly material with a favorable band gap (~2.1 eV) [38]. These are necessary requirements for massive applications in the solar energy conversion at an affordable cost. For the improvement of the hematite α-Fe_2O_3 as the photo-electrode material, M-doped α-Fe_2O_3 film (M = Cr, Mo, Pt, Ti) has been studied experimentally [39-42]. The first-principles studies on Co and Ni doped hematite film have also been performed [43]. They exhibit the higher photoelectrochemical (PEC) performance than that of the undoped samples. As the application of the photovoltaic (PV) material, however, it has been found that the potentially low-cost material does not have satisfactory performance in practice, which could be attributed to the relatively poor absorptivity and indirect band gap [35, 44]. To modify the electronic structures and transport properties of α-Fe_2O_3, the hematite doped with Al, Ti, and Cu have been investigated by the experimental and theoretical studies [45-47]. But no improvement in the performance has been achieved for hematite in solar energy conversion. It is well known that a direct band gap ranging from 1.30 eV to 1.60 eV is optimal for a solar cell material. The influence of different concentrations of isovalent sulfur (S) doping in the bulk hematite on the band structure and optical absorption has recently been investigated [48]. It elucidates that the α-$Fe_2O_{3-x}S_x$ with S concentration of ~5.6% has a direct band gap with a desirable value (~1.45 eV).

Hence, it is worth to further investigate the incorporation of S atom into α-Fe_2O_3. As an initial stage, the adsorption and substitution of S atom at the surface of α-Fe_2O_3 need to be understood. Firstly, a surface model should be obtained. The properties of the clean hematite α-Fe_2O_3 films have already been investigated. The electronic structure of the clean hematite α-Fe_2O_3 (0001) surface has been discussed theoretically in detail by W. Bergermayer *et al.* [49]. Under low and intermediate oxygen pressures the Fe-terminated surface is most stable but under high oxygen pressure the O_3-terminated surface is more stable. The electronic properties of the graphene-hematite interfaces have been studied [50]. The interaction mechanism between H_2S and the α-Fe_2O_3 (0001) surface [51] was studied by density functional theory (DFT) in order to remove H_2S from coal gas. Some recent studies with DFT also considered different metal atoms, *i.e.* Mg, Au and Pb, adsorption on the α-Fe_2O_3 (0001) surface [52, 53].

3.2 Computational details and models

All the calculations performed in this work are based on spin-polarized DFT as implemented in the Vienna *ab initio* simulation package (VASP) [54, 55]. The exchange-correlation energy is treated within the generalized gradient approximation (GGA) functional and parameterized by Perdew-Burke-Ernzerhofer (PBE) [56] functional. The electron-ion interaction is described by the projector augmented wave (PAW) potentials [24], treating Fe 3p, 3d and 4s, O 2s and 2p, and S 3s and 3p states as valence states. A plane wave basis with an energy cutoff of 400 eV is used and the convergence for energy is chosen as 10^{-5} eV. In order to describe the effect of the on-site coulomb repulsion of Fe-3d electrons more accurately, the exchange-correlation energy is treated by the GGA + U approach used by Dudarev *et al.* [57] with U=4. Full structural optimization is carried out until the force converged below 0.05 eV/Å. The search for the transition states (TSs) along the minimum-energy pathway (MEP) between two stable configurations is calculated using the climbing-image nudged elastic band (CI-NEB) method [58]. There are eight images used in the calculation.

To demostrate the accuracy of our computation setting, the structure of bulk hematite with a hexagonal prime cell consisting of six formula units is calculated first. Integrations over the first Brillouin zone (FBZ) are performed with a 5×5×5 Monkhorst-Pack [59] k-point grid. All possiple magnetic phases are considered. The global energy minimum state is an anti-ferromagnetic (AFM) phase with magnetic moment of $4.15\mu_B$ on each Fe atom. The optimized lattice constants of the bulk α-Fe_2O_3 (a=5.043 Å, c=13.729 Å) are in excellent agreement with experimental values (a=5.035 Å, c=13.747 Å) [29]. It has an indirect band gap with the value of 2.05 eV, in good agreement with the experimental and the previous results [29].

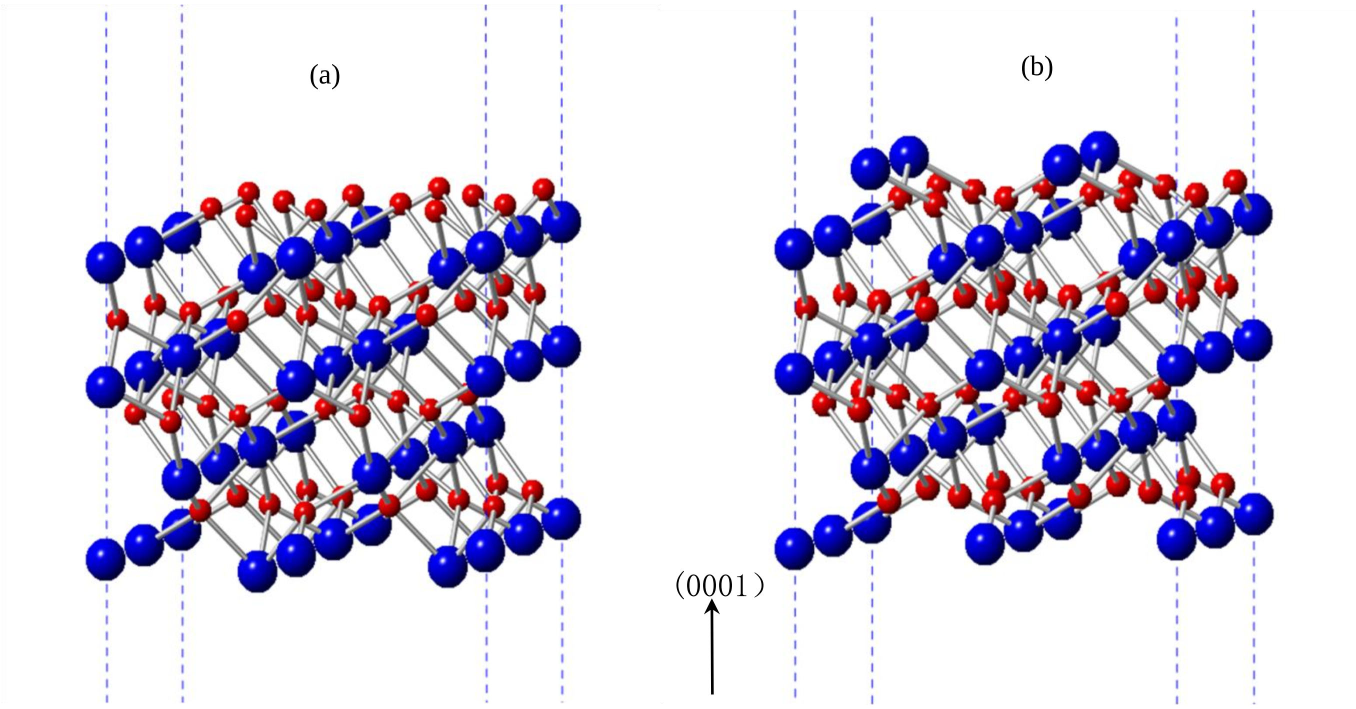

Figure 3.1. The 2×2×1 hematite (0001) surface. (a) is the film of type A. (b) is the film of type B. The Fe atoms are blue large balls and the O atoms are red small ones.

The hematite (0001) surface is a stable surface at oxygen partial pressure and ambient temperature [49]. The present work will focus on this surface. The (0001) surface is modeled by a thin film built of 12 atomic layers and a vacuum region of 15.0 Å normal to the film in a periodic boundary condition as shown in Fig. 3.1. In order to keep the stoichiometry for simplicity, there are two possible films for consideration. The film of type A is that one surface is terminated by Fe atoms while another surface is terminated by O atoms, as shown in Fig. 3.1(a). The film type B is that both sides of the surface are terminated by Fe atoms, as shown in Fig. 3.1(b). The FBZ of the 1×1×1 surface unit cell is sampled by 5×5×1 *k*-points. While for 2×2×1 surface supercell, a 3×3×1 k-points is employed. For the sake of accuracy, a double k-point mesh is also tested. The difference of the total energy is less than 0.01 eV. Whereas for all the density of states (DOS) calculations shown in this work, the double k-point meshes are employed. The electronic structure analyzed through the Bader charge analysis [60] has been used in the later discussions.

The adsorption energy is calculated as

$$E_{ads} = E_{tot}(X/film) - [E_{tot}(film) + E_{tot}(X)], \tag{3-1}$$

where $E_{tot}(X/film)$ is the total energy of the slab covered with the adsorbate X in its ground state, $E_{tot}(film)$ is the total energy of the bare substrate, and $E_{tot}(X)$ represents the total energy of the free adsorbate. By this definition, the more negative the E_{ads} is, the stronger the adsorption is.

3.3 Results and discussion

3.3.1 Clean α-Fe_2O_3 (0001) film

To investigate the stability of the films with two different types of termination, as shown in Fig. 3.1 (a) and (b), the total energies of each slab with various possible anti-ferromagnetic (AFM) arrangements and a ferromagnetic (FM) arrangement have been calculated. It is found that for both type A and type B films, after structural optimization, the total energy of the slab with an AFM phase is always lower than that with an FM one. The results also show that the total energy of type B film is 0.83 eV per formula unit lower than that of type A film by comparing their most stable configurations. It means that type B film with both sides terminated by Fe atoms is energetically the most stable film in the 12-layer film models. Cleaving energy per formula unit (E_c) of the films with respect to the bulk structure of hematite is calculated as,

$$E_c = \frac{E_{Film}}{n} - \frac{E_{Bulk}}{m}, \qquad (3\text{-}2)$$

where E_{Film} is the ground state total energy of the film and E_{Bulk} is the ground state total energy of the bulk hematite structure. n and m are the number of formula units in the super cells for each case used in the calculations. E_c for type B and type A films are 0.81 and 1.64 eV per formula unit, respectively, which indicates that type B film is more energetically favorable to synthesize than type A film. Therefore, the type B film is adopted in this study.

Table 3.1. The different possible magnetic arrangements of type B film compared by the relative total energies and the magnetization moments. A symbol ↑ or ↓ indicates the orientation of total magnetic moments of each Fe atomic layer.

Configurations	Magnetic arrangement of iron	Relative total energy per formula	Total magnetization per
AFM-1	↑↑↓↓↓↓↑↑	0.32	-0.05
AFM-2	↑↑↓↓↑↑↓↓	0.27	0.00
AFM-3	↑↑↑↑↓↓↓↓	0.51	0.00
AFM-4	↑↓↓↑↑↓↓↑	0.00	-0.06
AFM-5	↑↓↑↓↑↓↑↓	0.25	0.00
FM	↑↑↑↑↑↑↑↑	0.61	9.67

The results of the various magnetic arrangements of type B are shown in Table 3.1, including FM and all possible AFM configurations. And with the AFM-4 configuration, the film has the lowest total energy and almost zero net magnetic moment. At the same time the lattice parameter a is also optimized, which is ~3.0% larger than its value of the bulk structure. Hence, it is understandable to find that the length of all of the Fe-O bonds is increased by 2.1%-2.4% except those of the terminated Fe atoms with their neighboring O atoms. The bond length of the terminated Fe's with the underneath O atoms is decreased by ~6.5%. In the following studies, the most stable type B film (AFM-4) with the optimized lattice constant will be used.

The density of states (DOS) of the film is shown in Fig. 3.2, together with that of the bulk hematite for comparison. There are some differences between the film and the bulk in Fig. 3.2. The DOS of the film between spin-up and spin-down is asymmetric. This is due to the asymmetrical atomic magnetic moment arrangement, *i.e.* AFM-4 in Table 3.1, resulting from that both sides are terminated by spin-up Fe atoms. Obviously, there are new spin-down states at the energy level at about 1.43 eV above the valance band minimum (VBM). Due to the new states, though unoccupied, the energy band gap is dicreased from ~2.05 eV of the bulk to ~1.43 eV for the film. The new surface states result from the Fe-3d states of the terminated Fe atoms. In addition, there is a symmetry broken for spin up and down in the valence bands of the film. The DOS from -5.0 eV to 0.0 eV are shifted between the spin-up states and the spin-down states. Fig. 3.2 also shows that the VBM is dominated mainly by O-2p states, while the lowest conduction band edge is primarily Fe-3d states in character, similar to the situation of the bulk. The magnetic moment of the terminated Fe atom on the surface is ~4.02μ_B, discreased by 3.6% from the value of the inner Fe atoms. But the film still keeps the AFM orientation.

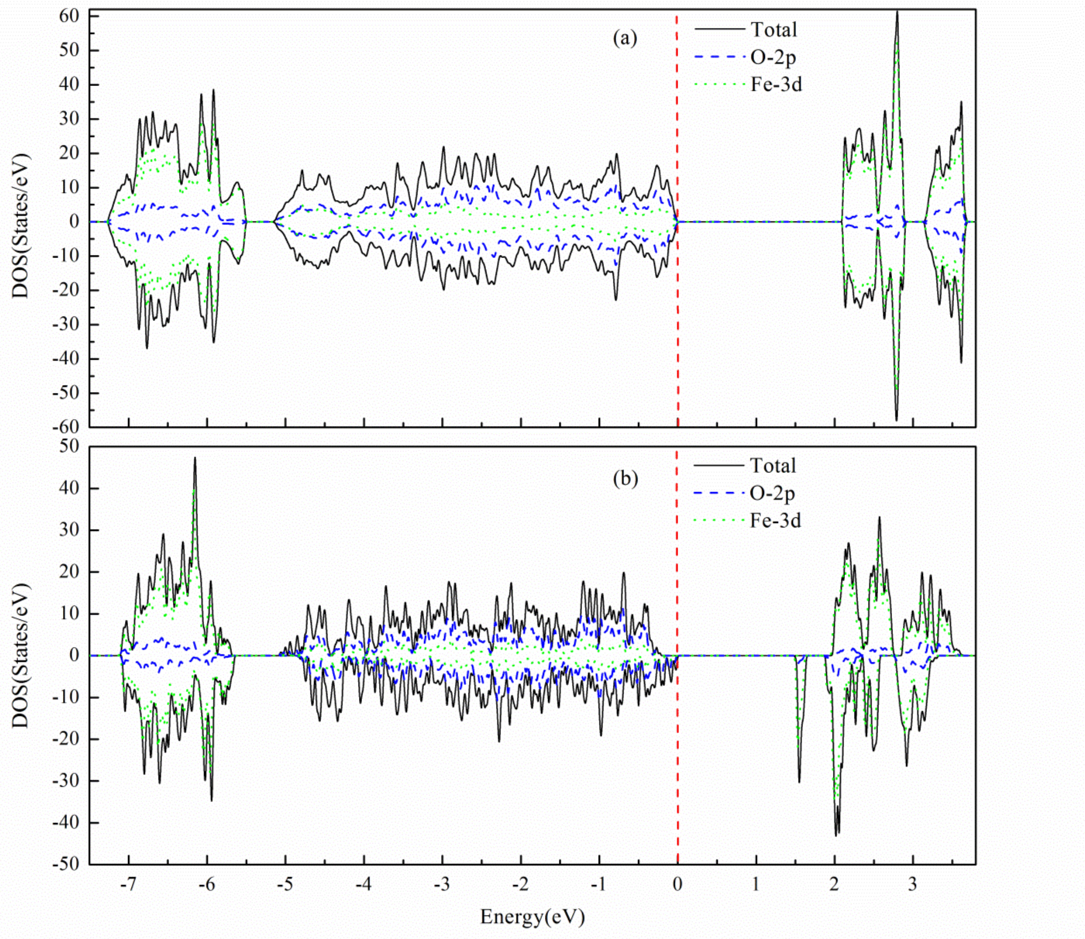

Figure 3.2 The density of states (DOS) of the bulk hematite (a) and the (0001) film (b). The positive and negative value represent spin up and spin down, respectively. The zero energy is the valence band maximum (VBM).

3.2 S-adsorption on the α-Fe_2O_3(0001) surface

According to the previous theoretical study, the isovalent doping of S in the bulk α-Fe_2O_3 can modify significantly the band edges near the band gap [48]. It is important to understand the feasibility of the incorporation of sulfur into α-Fe_2O_3. The initial stage of the doping process could be the adsorption of S on the α-Fe_2O_3 surface. For a sulfur adatom adsorption on the suface of the film model discussed in the previous section, various sites have been examined. They are top (T) sites of the Fe or O atoms, hollow (H) sites and several bridge (B) sites, as shown in Fig. 3.3.

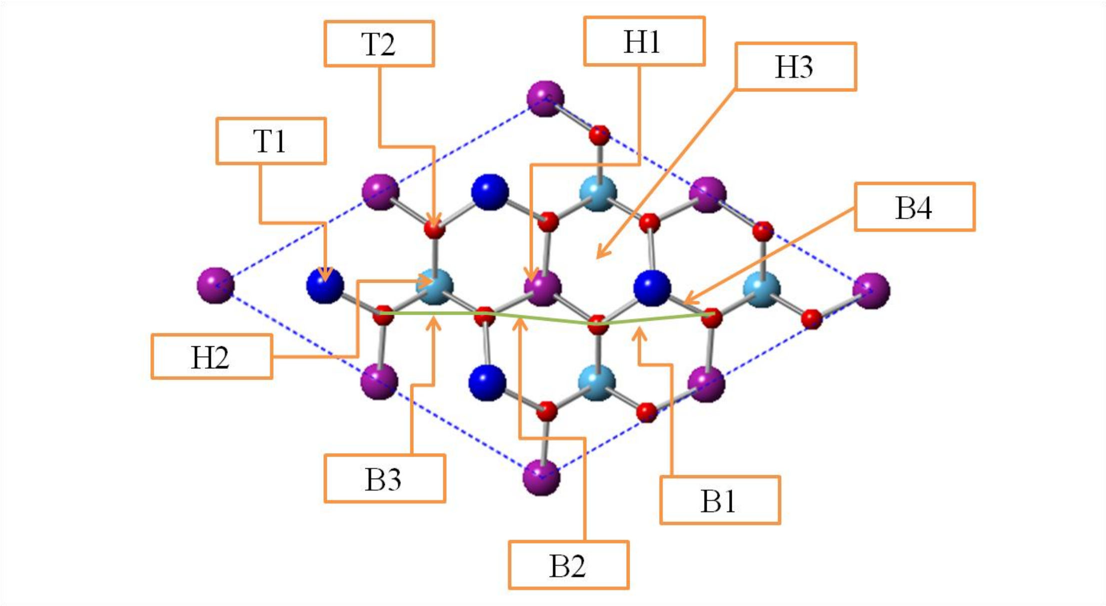

Figure 3.3 The top view of various sites for S-adsorption. The small balls are O atoms below the top layer. All the big balls are Fe atoms. The blue color is the top layer Fe's. The purple color is the second layer Fe's. The cyan color is the third layer Fe's. The lowest-energy adsorption site for S is H2.

There are three Fe atom layers and one O atom layer are shown for S-adsorption in Fig. 3.3. The top-most Fe atom layer is named as Fe(I) (blue), and the second Fe atom layer is called as Fe(Ⅱ) (purple) and the third Fe atom layer is Fe(Ⅲ) (cyan). The O atom layer is between the Fe(I) layer and Fe(Ⅱ) layer. T1 and T2 are the top sites of the Fe(I) and O atom, respectively. H1, H2, and H3 are three hollow sites of O atoms which form the equilateral triangle, but the bottom atoms under the hollow sites are the Fe(Ⅱ), the Fe (Ⅲ) and an O atom from even deeper layer, respetively. B1, B2, and B3 are three bridge sites of O atoms. These bridge sites are across two neighboring oxygen atom in the same layer. B4 is a bridge site between the bonded O atom and Fe(I) atom. Table 3.2 lists only the stable sites at which S atom does not relax away from the initial position after the optimization. In Table 3.2, the relative energy is measured from one of the most stable site, which is H2.

Table 3.2. The adsorption sites comparison with the relative energy ΔE_{tot}, the nearest neighbors of the adsorbate atom and their distance after the geometry optimization.

Site	ΔE_{tot} (eV)	First nearest neighbors and the distance (Å)		Second nearest neighbors and the distance (Å)	
T1	1.87	Fe	2.28	O	3.44
H2	0.00	O	1.56	Fe	3.18
T2	0.85	O	1.74	Fe	2.26
B3	1.005	O	1.64	Fe	2.50
H3	2.38	O	1.57	Fe	2.52

Fig. 3.4 gives the side view of the S-adsorption on the most stable site on the surface. The adsorption energy of the most stable adsorption site calculated is -4.20 eV using Eq. (3-1). As listed in the second row of the Table 3.2, for the most stable adsorption site (H2), the nearest neighbors of the adsorbate sulfur atom are the three oxygen atoms, forming an equilateral triangle, with the S-O distance of 1.56 Å. As a result, the three O atoms move upwards by about 0.49 Å. The distance between the adsorbate S atom and the second nearest neighbor, which is the Fe (I) atom on the first layer, is much larger, about 3.18 Å.

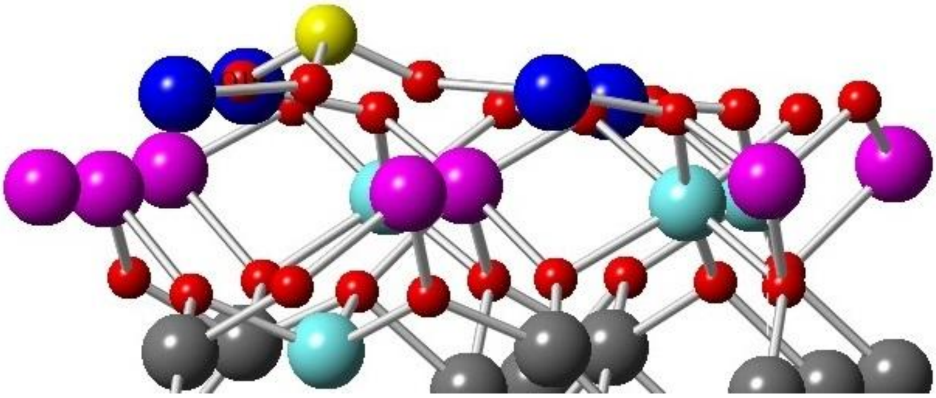

Figure 3.4. The side view of the most stable site for S-adsorption. The bigger balls are Fe (I) (blue), Fe (II) (purple), and Fe (III) (cyan) atoms. The smaller balls are O atoms. The middle size ball is the S adatom.

Surprisingly, the S adatom prefers to bond with the three O atoms on the surface, in the centre of the equilateral triangle formed by the three O atoms. In other words, the S atom would like to form a SO_3 cluster with the three O atoms on the surface. After the adsorption of sulfur atom, due to the bonding of the three O atoms and S adatom, the original bonds between the three O atoms and the underneath Fe atom, Fe (Ⅲ), are broken, causing a significant downward displacement of the Fe (Ⅲ) by ~1.95 Å. And the magnetic moment of the Fe (I) atom which bonds with the O atoms in SO_3 is decreased by 13.6%.

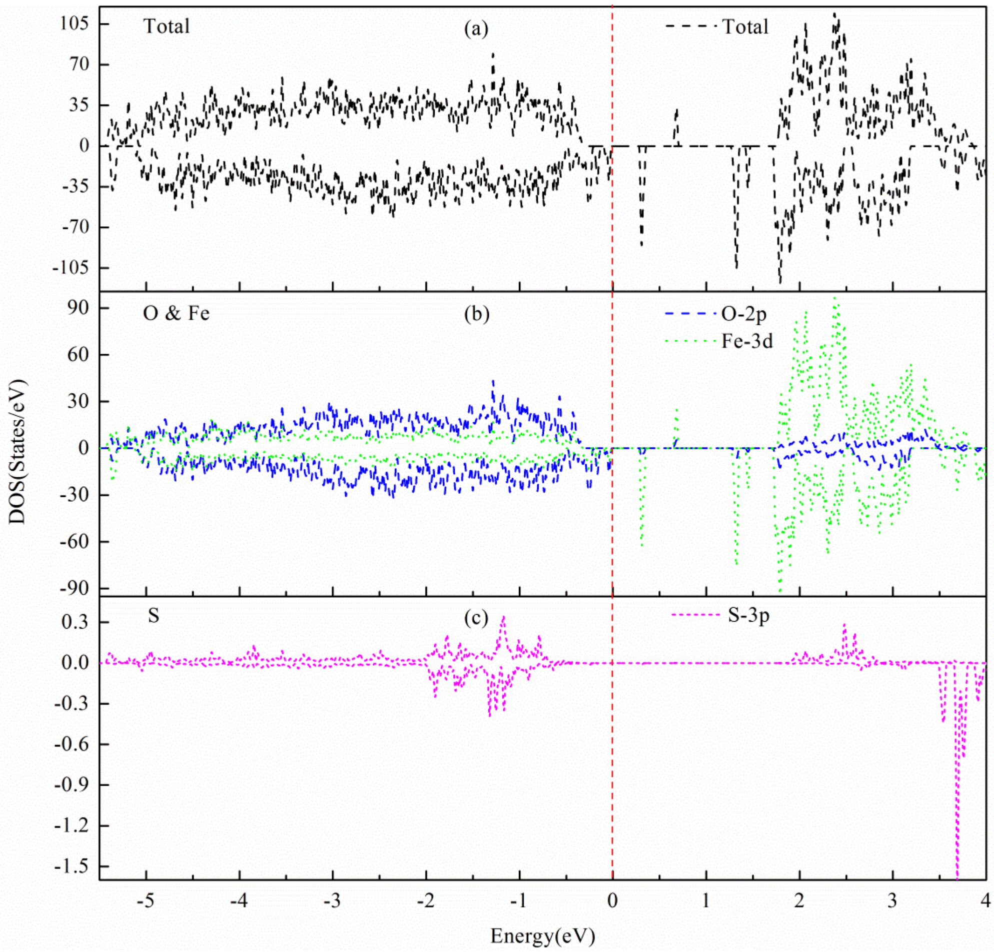

Figure 3.5. The density of states (DOS) of the S-adorption on hematite α-Fe_2O_3 (0001) film: the total DOS of the film with the S adsorbed (a); the projected DOS of the Fe and O atoms (b); the projected DOS of the S adatom (c). The zero energy is aligned with the clean film with respect to 1s core level of a remote O atom.

In Fig. 3.5, the total and projected DOS for the different atoms on the most stable site of the film are presented. The top of the valence bands and the bottom of the conduction bands are dominated mainly by O-2p states and Fe-3d states, respectively, which is unchanged from that of the clean film. Comparing with the DOS of the clean film, the S adsorption induces two additional gap states in the band gap discussed in section 3.3.1. They are not directly coming from the S atom. The main contribution of the states in the band gap is from the Fe atoms at the nearby of the S adatom. According to the analysis of the projected DOS of each atom, which is not shown here, the lower spin-down peak is contributed by the three second nearest neighbor Fe (I) atoms shown in Fig. 3.4. And the spin-up peak is contributed by the Fe (III) atom which has a significant downward displacement as shown in Fig. 3.4.

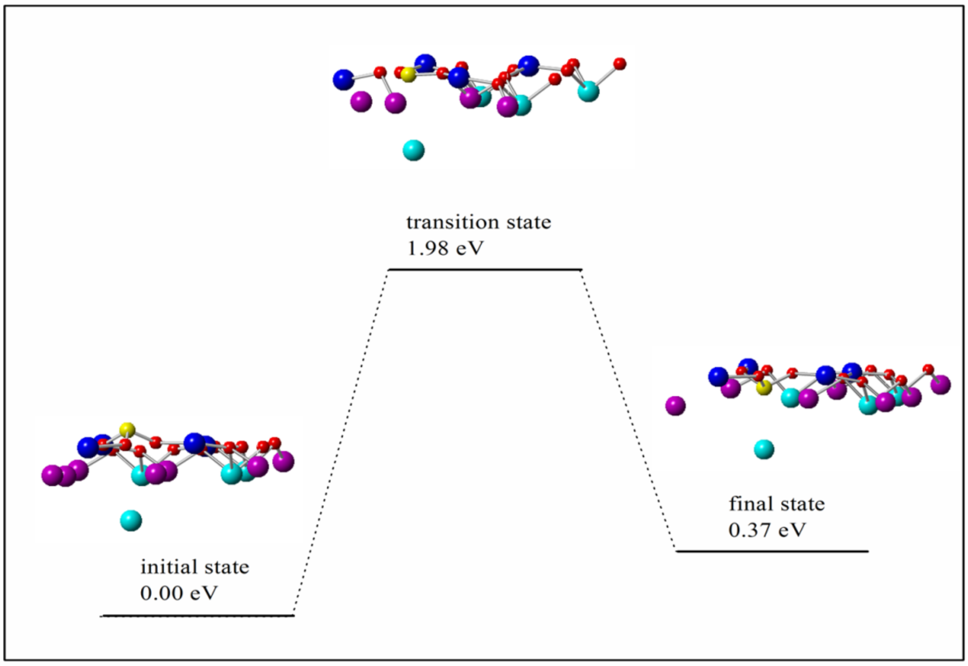

Figure 3.6. The schematic potential energy profiles for the S atom diffusion on the hematite (0001) film. The side views of structures of the initial state, transition state and final state are given.

It is also important to understand the migration of the S adatom on the hematite α-Fe_2O_3 (0001) film. It is found that the S atom remains to bond with the three O atoms after it is placed beneath the plane of the oxygen triangle. The total energy of the configuration after geometry optimization is 0.37 eV higher than that of the most stable S-adsorption configuration. The diffusion of the S adatom is evaluated and the transition state along the minimum-energy pathway is searched using the climbing-image nudged elastic band (CI-NEB) method. As shown in Fig. 3.6, the most stable S-adsorption configuration and the configuration described above are selected as the initial state and the final state. Obviously, the diffusion goes through a barrier of energy from the initial state to the final state. The pathway and the transition state are also shown in Fig. 3.6 and the energy barrier is about 1.98 eV. In Fig. 3.6, for the transition state, the sulfur atom is co-plane with the three O atom triangle. But due to the larger size of sulfer atom, one oxygen atom is pushed a little further than the other two O atoms.

3.3.3 S-doping in the α-Fe_2O_3(0001) film

To study the sulfur atom doping in the film, only the S substitution of O atom is considered. For our hematite film model, as shown in Fig. 3.1 (b), there are four oxygen layers, with a symmetry. For the study of the sulfur doping in the film, the substitutions of oxygen atom on the first oxygen layer and the second oxygen layer are considered. The S atom substitution of the first layer O atom is energetically 0.56 eV lower than that of the substitution of the second layer O atom. In other words, it is more stable to substitute of the sulfur atom for the surface oxygen atom. This indicates that S atom prefers to stay at the surface. The total and projected DOS of the S-doping in the first oxygen layer is given in the Fig. 3.7. It shows that the band gap is reduced to ~1.26 eV from ~1.43 eV of the clean film, similar to the S-doping in bulk Fe_2O_3 [48]. The maximum of the valence band is dominated by O-2p and S-3p states, while the bottom of the conduction bands is mainly contributed by Fe-3d states, similar to S-doping in the bulk.

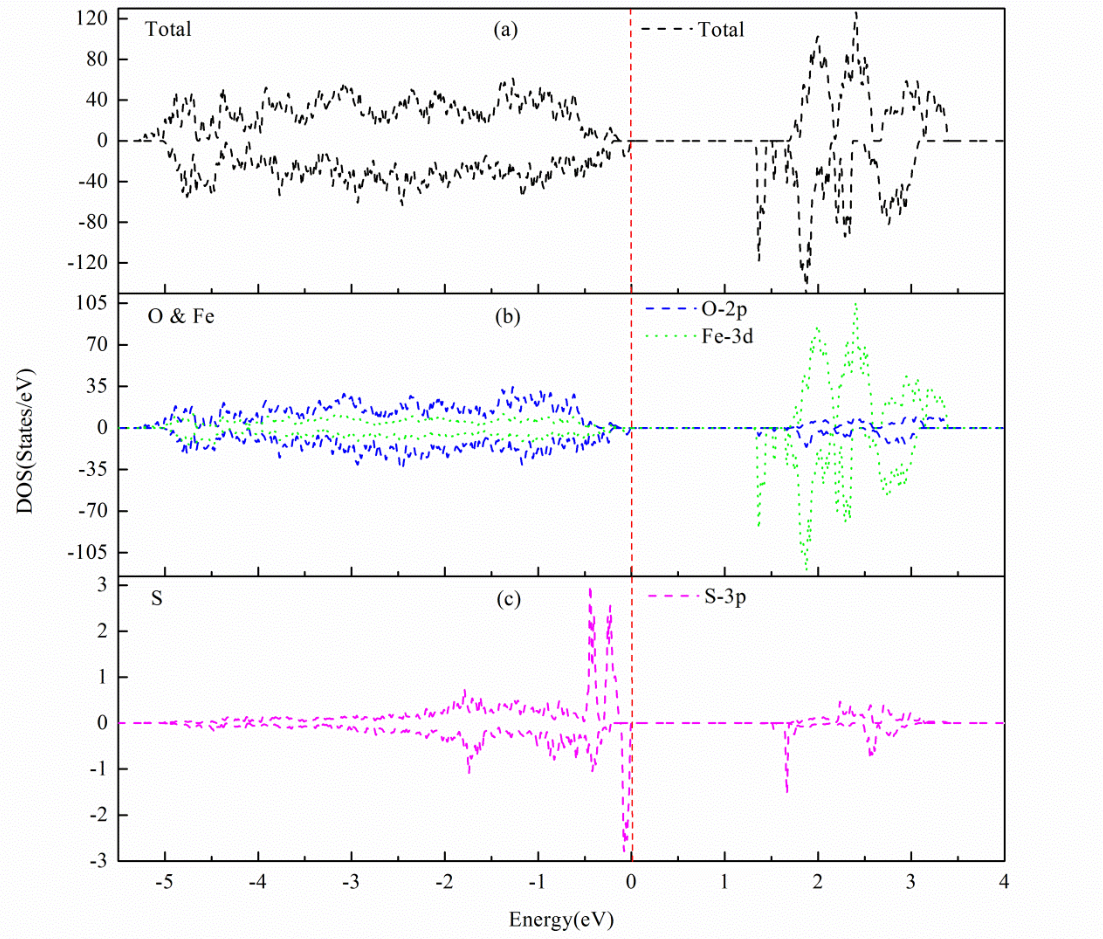

Figure 3.7. The density of states (DOS) of the S-doing in the first oxygen layer of hematite α-Fe_2O_3 (0001) film: the total DOS (a); the projected DOS for the Fe and O atoms (b); the projected DOS for the S atom(c). The zero energy is aligned with the clean film with respect to 1s core level of a remote O atom.

The feasibility of the isovalent S substitution in the film of the hematite α-Fe_2O_3 has been investigated by calculating the formation energy according to the formula

$$E_{form} = E_{tot}(doped\ \ film) - E_{tot}(clean\ \ film) + \mu_O - \mu_S, \qquad (3\text{-}3)$$

where $E_{tot}(doped\ \ film)$ and $E_{tot}(clean\ \ film)$ are the total energies of the S-doped and the clean hematite slab, respectively. μ_S and μ_O denote the chemical potentials of sulfur and oxygen atom, respectively. The μ_O can be obtained from the ground-state total energy of the

O_2 molecule ($\mu_O = \frac{1}{2}\mu_{(O_2)}$), while the μ_S is calculated from the α-S_8. The calculated formation energies for the first and second layer are 2.29 eV and 2.85 eV per sulfur substitution, respectively. So it is relatively hard for S to be doped into the clean Fe_2O_3 film.

For the S-adsorption and the isovalent S-doping, the Bader charge analysis has been applied. It is found that the Bader partial charge of the S ion is ~3.65e and ~6.67e for S-adsorption and S-doping, respectively. It means that the S acts as a cation in the S-adsorption position, while it presents anionic behavior in the S-doping condition.

In summary, the structural and electronic properties of the clean hematite α-Fe_2O_3 (0001) film have been studied by DFT + *U* method. The film terminated by Fe atoms on both sides with the AFM arrangement is the most stable one. Based on this film, the sulfur atom adsorption has been studied. For a sulfur atom adsorption on the suface of this model, the S adatom prefers to bond with the three O atoms on the second layer of the surface, in the centre of the equilateral triangle formed by the three O atoms. The results of the adsorption by S atom at the α-Fe_2O_3 (0001) surface suggest that S atom prefers to stay at the surface, and there is a high barrier about 2 eV for the sulfur atom penetrate into the film.

Chapter 4

TiO_2 single-walled nanotubes from hexagonal sheet

4.1 Introduction

Metal oxides have been investigated significantly both experimentally and theoretically due to their rich physical and chemical properties. As an important member of them, titanium dioxide (TiO_2) has drawn more and more attention of researchers, and has been studied broadly in a wide range of applications, such as air and water pollution, photocatalysis, hydrogen storage and production, and novel solar cells [61-66].

Photocatalysis, in which the inexhaustibly abundant, clean, and safe energy of the sun can be harnessed for sustainable, nonhazardous, and economically viable technologies, is a major advance in its application. Titanium-oxide materials in different types and forms have shown great potential as ideal and powerful photocatalysts for various significant reactions due to their chemical stability, nontoxicity, cheap availability, and photocorrosion [67, 68]. It has three common polymorphs including rutile, anatase, and brookite [69-71]. The first two polymorphs have been studied extensively by experimental and theoretical methods. Technologically important anatase and rutile TiO_2 have been reported as the wide band gap semiconductors with band gap values of 3.2 eV [72] and 3.0 eV [73], respectively. However, the large band gap energy and massive recombination of photo-generated charge carriers limits its photocatalytic efficiency. In order to utilize a larger fraction of the solar spectrum for enhancing the photocatalytic process, tuning the band gap of TiO_2 to the visible region is a vital task when designing the materials. For this purpose, TiO_2 is modified by various strategies, such as coupling with other semiconductors, surface sensitization by organic dyes, metal ion or nonmetal ion doping, and co-doping with two or more foreign ions [74-80]. Coupling the TiO_2 with SnO_2 was reported to enhance the charge separation and then the photocatalytic activity [81]. For the dye sensitization of TiO_2, although it was theoretically possible to utilize the longer wavelength light in the aqueous electrolyte solutions, it had the practical problems that most organic dyes would be far too unstable under the solution condition [82].

On the other hand, promising two-dimensional (2D) semiconductors have been investigated for potential applications in nanoelectronics, optoelectronics, and catalytic and gas-sensing devices [83-86]. Titanium oxide 2D nano films are desirable for the catalytic application due to their large surface areas and high reactivities. The anodizing approach is able to build the titanium oxide 2D nano film with controllable size, good uniformity, and conformability over large areas at low cost. It was found that during anodization the color of the titanium oxide layer normally changed from purple to blue, and then light green, and finally light red [87], indicating a reduction of the band gap. The titanium oxide nanotube arrays were regularly obtained under anodizing voltages ranging from 10 to 40 V.

4.2 Computational details and models

All the calculations performed in this work are based on the density functional theory (DFT) as implemented in the Vienna *ab initio* simulation package (VASP) [54, 55]. The exchange-correlation energy is treated within the generalized gradient approximation (GGA) functional and parameterized by Perdew-Burke-Ernzerhofer (PBE) [56] functional. The electron-ion interaction is described by the projector augmented wave (PAW) [24] potentials, treating Ti 3p3d4s, O 2s2p, and S 3s3p states as valence states in the pseudopotetial calculations. A plane wave basis with an energy cutoff of 400 eV is used and the convergence for energy is chosen as 10^{-5} eV. Integrations over the first Brillouin zone are performed using the Monkhorst-Pack k-point grids [59] of 1×1×13 for (n,n) nanotubes and 1×1×11 for (n,0) nanotubes, respectively. In order to describe the effect of the on-site coulomb repulsion of Ti-3d electrons more accurately, the exchange-correlation energy is treated by the GGA + U approach used by Dudarev *et al*. [57] with U=7 eV.

To check the accuracy of our computation setting, the structural and electronic properties of the bulk rutile and anatase have been studied. The full structural optimization is carried out until the force converged below 0.01 eV/Å. For rutile TiO_2, the optimized lattice parameters (a= 4.636, c= 3.040) are just 0.91% and 0.28% larger than the experimental values (a= 4.594, c= 2.958) [88], respectively. The rutile TiO_2 has a calculated indirect band gap with the value of 2.75 eV, a little bit smaller than that of the experimental measurement (~3.00 eV) [89]. While for anatase TiO_2, the optimized lattice parameters (a= 3.865, c= 9.604) are just 2.1% and 0.96% larger than the experimental values (a= 3.785, c= 9.512) [88], respectively. The anatase TiO_2 has a calculated indirect band gap of 2.97 eV, slightly smaller than the experimental measurement (~3.20 eV) [90]. Although the hybrid functional calculation with HSE approach [91, 92] can obtain closer values to the experimental measurement, it is highly computationally expensive for a large system such as the nanotubes considered here. Therefore, further calculations will be carried out with the GGA + U approach.

4.3 Results and discussion

4.3.1 The two-dimensional TiO_2 sheets

Since the construction of a single-wall nanotube model is done by rolling a corresponding single molecular layer which is called nanosheet hereafter, the TiO_2 2D sheets are studied first. Various low-index planes of both rutile and anatase crystals have been considered. A new 2D sheet structure with a hexagonal ABC PtO_2 geometry, known as hexagonal ABC (HexABC) sheet , is also considered [93, 94], though there is no bulk HexABC TiO_2 structure in nature. The geometries of the sheets have been fully optimized. Their total energies per formula unit are listed in Table 4.1. It is found that the energy of the TiO_2 HexABC sheet is the lowest one. It also means that the TiO_2 HexABC sheet is the most stable sheet among all the sheets considered in the Table 4.1, and so the TiO_2 HexABC sheet will be used to construct the nanotubes in the following studies. The TiO_2 HexABC sheet structure have been obtained experimentally when the ultrathin titanium oxide films were grown on the substrates of Cu(100) and Fe/Cu(100) [95] as well as Ru(0001) [96]. The monolayer films were obtained by evaporation of Ti atoms on the oxygen chemisorbed substrates, followed by annealing in an O_2 environment. The hexagonal geometry of TiO_2 has also been observed recently by the atomic-resolved STM from the reconstructed of rutile (011) surface [97].

Table 4.1 The relative total energy per formula unit, ΔE, of each TiO_2 sheet. R refers to rutile and A refers to anatase.

Sheet	ΔE (eV)
R(110)	1.037
R(001)	0.828
R(100)	0.498
R(101)	0.661
A(001)	2.765
A(010)	0.450
A(110)	1.548
A(101)	0.119
HexABC	0.000

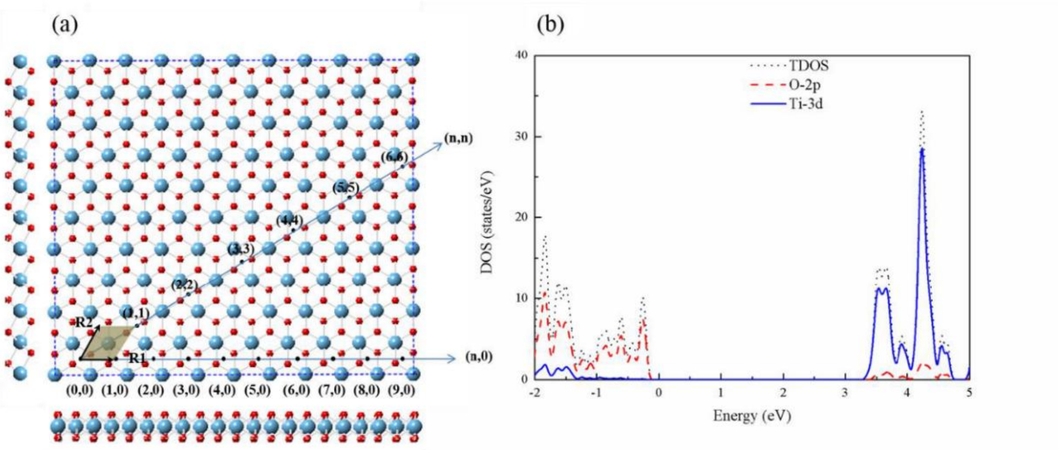

Figure 4.1. (a) The top and both side views of the TiO_2 HexABC sheet, together with the index of formation of various TiO_2 nanotubes. The bigger blue balls are the Ti atoms and the smaller red balls are the O atoms. The unit cell of the TiO_2 HexABC sheet highlighted in the gray is defined by the primitive lattice vectors **R1** and **R2**. (b) The density of states of the TiO_2 HexABC sheet, with the projection values of O-2p and Ti-3d states.

In order to investigate the TiO_2 nanotubes formed with the most stable sheet, the TiO_2

HexABC sheet, the structural and electronic properties of the nanosheet have been studied. In Fig. 4.1 (a), it shows the top and side view of the TiO_2 HexABC sheet and the index corresponding to the formation of the various TiO_2 nanotubes. The same scheme as carbon nanotubes is used with zigzag nanotubes defined by a rollup vector along the (n,0) direction and armchair nanotubes defined by a rollup vector along the (n,n) direction. As shown in Fig. 4.1 (b), from the density of states (DOS), the TiO_2 HexABC sheet has a gap with the value of 3.54 eV. It also shows that the upper edge of the valence band is dominated mainly by O-2p states, while the bottom of the conduction band is primarily Ti-3d states in character.

4.3.2 The single-wall TiO_2 nanotubes from the HexABC sheet

As an example, the cross-sections of the armchair-like nanotube (8,8) and zigzag-like nanotube (8,0) are shown in Fig. 4.2 (a) and (b), respectively. In the following discussion, the distance from the axis of the tube to a Ti atom is defined as the radius of the nanotube, denoted as *r*.

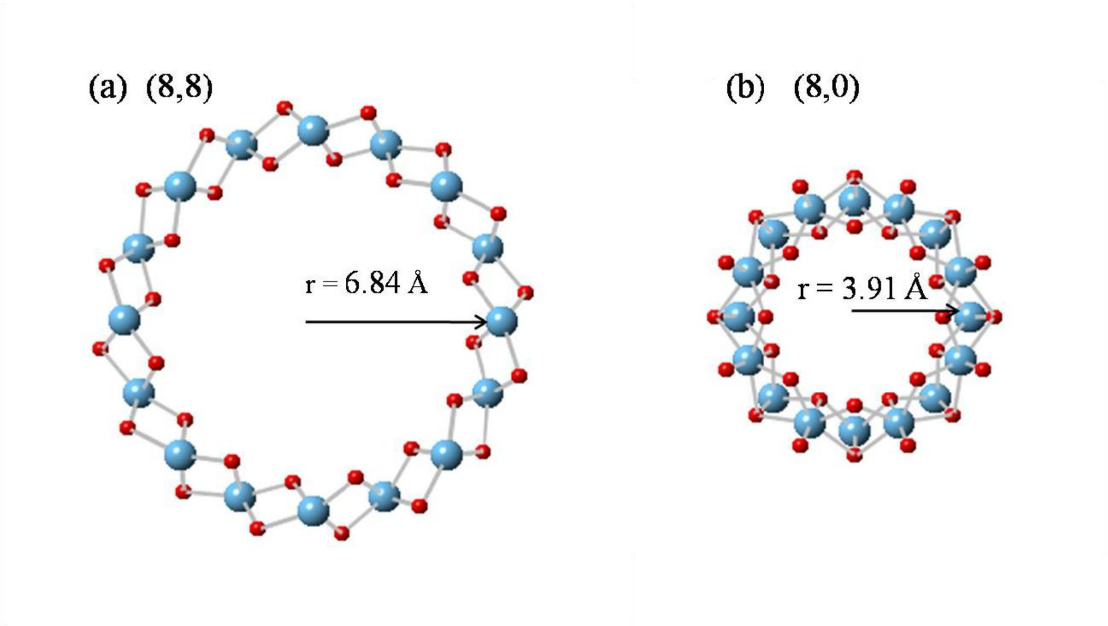

Figure 4.2. (a) One-layered TiO_2 HexABC nanotube with chirality indices (8,8), cross-section. (b) One-layered TiO_2 HexABC nanotube with chirality indices (8,0), cross-section. The bigger blue balls are the Ti atoms and the smaller red balls are the O atoms.

First, the nanotube strain energies, E_{strain}, are calculated for both types from n=6 up to n=20. It is defined as

$$E_{strain} = E_{nt} - E_{sheet} \quad , \qquad (4\text{-}1)$$

where E_{nt} is the total energy per formula unit of the nanotube, and E_{sheet} is that of the sheet. In Figure 4.3 (a), the strain energies of TiO_2 HexABC nanotubes with different chirality indices

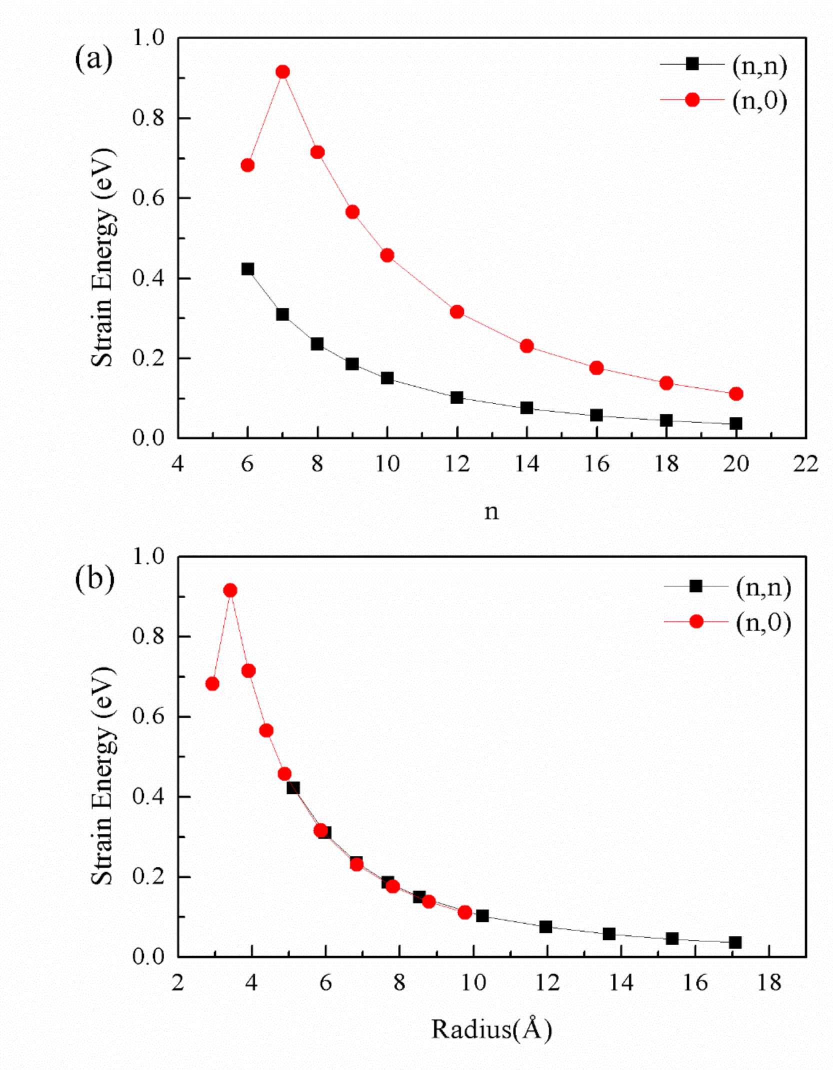

Figure 4.3. (a) The nanotube strain energies with chirality indices, (n,0) and (n,n) with n=6, 7, 8, 9, 10, 12, 14, 16, 18, 20. (b) The nanotube strain energies with different radii for both (n,0) and (n,n) indices.

are plotted. The (n,n) curve starts at a lower energy, 0.42 eV, and is flatter in comparison to the (n,0) curve, which starts at 0.68 eV. With the increase of the n value, the strain energy of the two types of nanotubes is decreased, and the (n,n) value is always below that of the (n,0) with the same n value. It also shows that both curves converge to approximately the same theoretical value of zero with the increase of n. The strain energy curves of these two types of TiO_2 nanotubes with different radii, *r*, are also presented in Fig. 4.3 (b). It is appropriate to point out that the (n,n) nanotubes have larger radii than those of (n,0) nanotubes with the same

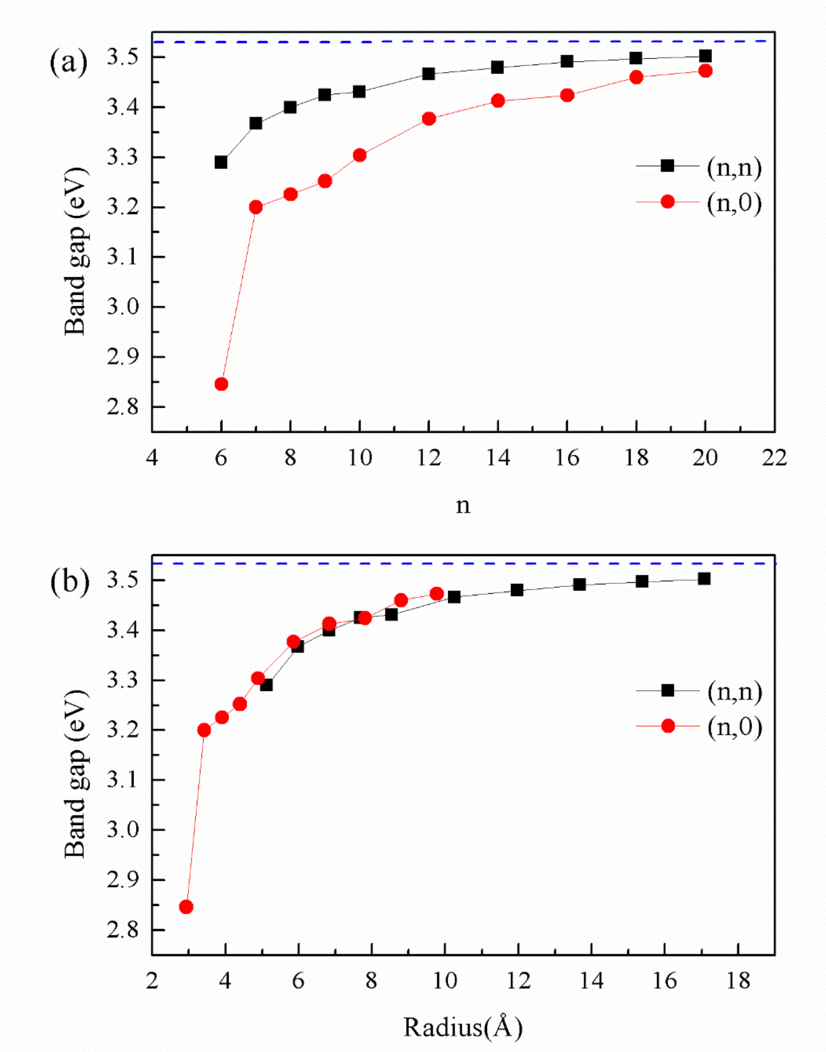

Figure 4.4. (a) The nanotube band gap values varying with indices n for both (n,0) and (n,n) chirality. (b) The nanotube band gap values varying with radii. The blue dash line is the band gap value of the TiO_2 HexABC sheet as a reference.

n value as demonstrate in Fig. 4.2. It also shows that with the increase of *r*, the strain energy is decreased monotonically, except for the special case of nanotube (6,0) which will be discussed in detail later. Similar trends for the strain energy of carbon and BN nanotubes were reported earlier [98-99].

The band gap values of the nanotubes with the different n are shown in Fig. 4.4 (a). With the increase of n, the band gap is increasing monotonically, approaching the band gap value of the TiO_2 HexABC sheet (3.53 eV), which is actually higher than the bulk band gap values of both rutile and anatase. The larger the strain is, the smaller the band gap is. A (n,0) nanotube always has a lower band gap value than that of (n,n) with the same chirality indices. However, the (6,0) tube has a significant lower value of ~2.85 eV. In Fig. 4.4 (b), it shows that the band gap values are basically increased with the increase of the radius *r*. When the value of *r* increases to the largest value, 17.09 Å for the (20,20) nanotube, the band gap value reaches the largest value 3.50 eV, just below that of the nanosheet. There is a trend that when the *r* is larger than 7 Å, the curve of the band gap values becomes flatter than that of the smaller size nanotubes, consistent with the trend in the strain energies. The (6,0) nanotube has the smallest band gap among all the calculated nanotubes in this work. The value is not in the visible and red light region which is observed in the experimental work [94]. There could be some meta-stable structures formed or some impurity element introduced during the experiment.

As the results above shown, the nanotube (6,0) is a special one in the two types of the nanotubes studied in this work. This tube has undergone substantial reconstruction. The cross-section of nanotube (6,0) unrelaxed and with reconstruction are shown in Fig. 4.5 (a) and (c), respectively. Indeed, in nanotube (6,0), the coordination number of one third of the oxygen and titanium atoms is two (O_{2f}) and six (Ti_{6f}), respectively. And from the graph, it could be easily found that the oxygen atoms (O_{2f}) are located outside of the Ti atom layer of the (6,0) nanotube. The coordination number of the other two thirds of the oxygen and titanium atoms is three (O_{3f}) and five (Ti_{5f}), respectively. It should be noted that all oxygen and titanium atoms in the other nanotubes, including the unrelaxed (6,0) nanotube, and even

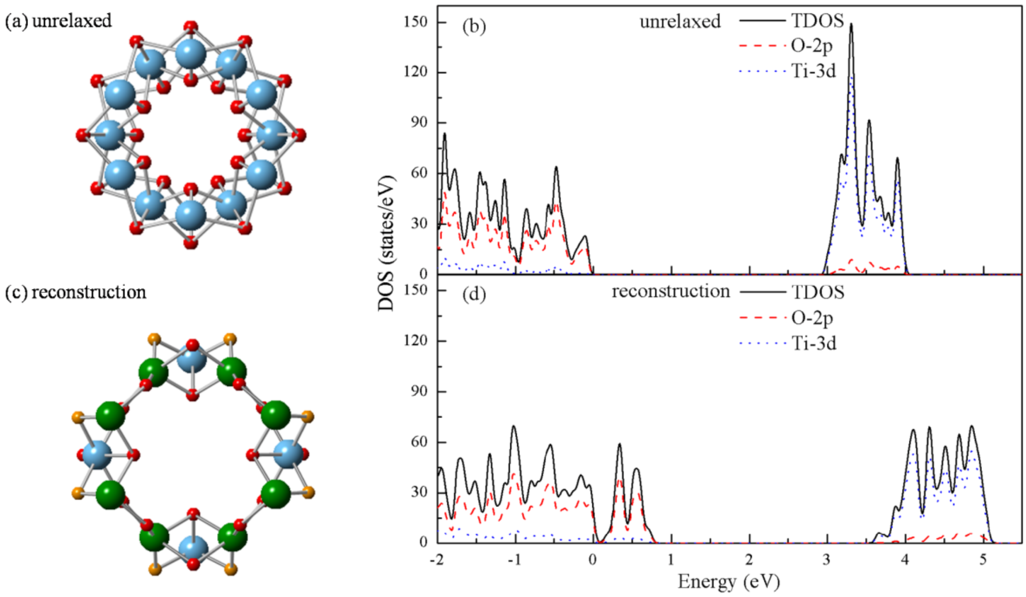

Figure 4.5. The cross-section view (a) and the density of states (DOS) (b) of the unrelaxed (6,0) nanotube. The blue balls are the Ti atoms and the red balls are the O atoms. The cross-section view (c) and the DOS (d) of the (6,0) nanotube with reconstruction. The bigger green balls are the Ti_{5f} atoms and the bigger blue balls are the Ti_{6f} atoms. The smaller orange balls are the O_{2f} atoms and the smaller red balls are the O_{3f} atoms. The zero energy is the valence band maximum of the unreconstructed (6,0) nanotube. The red dash line represents the O-2p states and the blue dot line represents the Ti-3d states.

the TiO_2 HexABC sheet are O_{3f} and Ti_{6f}, which are the same as those of the bulk TiO_2, anatase or rutile.

Obviously, the substantial structural change of the (6,0) nanotube causes a significant reduction of the band gap, from ~3.53 eV of the sheet value to ~2.85 eV. In Fig. 4.5 (d), the projected density of states (PDOS) of the nanotube (6,0) shows that the top of the valence bands are dominated by O-2p states, while the bottom of the conduction bands are mainly from Ti-3d states, similar to that of the TiO_2 HexABC sheet. From the Fig. 4.5 (b) and (d), it could be found that the shift-up of the top of valance bands mainly contributed by the O-2p states causes the decrease of the band gap value.

4.3.3 The sulfur substitution of oxygen and adsorption with the TiO_2 (6,0) nanotube

As plotted in Fig. 4.4, the band gap value of (6,0) is the smallest one among all the nanotubes studied in this work. It is also the only one below 3.0 eV. Therefore, the isovalent substitution of oxygen by sulfur (S) and its adsorption on the (6,0) nanotube are investigated for the chance of further reduction of the band gap. For these calculations, the supercell size is doubled in the *z*-direction.

4.3.3.1 The S substitution of oxygen with the (6,0) nanotube

There are 3 different possible substitution sites for the S substitution of oxygen in the (6,0) nanotube. For the inner oxygen layers, there is one type of the S substitution with O_{3f}. For the outer oxygen layers, there are two types of oxygen atoms (O_{2f} and O_{3f}), so there are two different sites for the S substitution of oxygen.

Table 4.2. The relative total energy about the sulfur (S) substitution of oxygen with the TiO_2 (6,0) nanotube. The total energy of the most stable doping site (Out_O_{2f}) is set as zero eV.

S-substitution sites	Relative total energy ΔE_{tot} (eV)	First nearest neighbors and distance (Å)		Second nearest neighbors and distance (Å)	
Out_O_{2f}	0.000	Ti	2.31	Ti	2.53
Out_O_{3f}	0.419	Ti	2.33	Ti	2.58
In_O_{3f}	0.380	Ti	2.40	Ti	2.54

In Table 4.2, the relative energy is measured from the most stable site, Out_O_{2f}, which is the replacement of the O_{2f} at the outer oxygen layer. The cross-section and side view of the most stable structure for the S substitution in the (6,0) nanotube are shown in Fig. 4.6 (a) and (b), respectively. The first and second nearest neighbors of the dopant S are the Ti atoms, with the bond length of 2.31 Å and 2.53 Å, respectively. Fig. 4.6 (c) shows the total density of states (TDOS) and PDOS of the most stable S substitution in the (6,0) nanotube. From the TDOS, it can also be observed that the band gap value is decreased to 1.84 eV. There are some new occupied states above the original valance bands of the clean (6,0) nanotube due to the substitution of an O atom by the S atom. Fig. 4.6 (d) inset also shows that the main contribution of the new states in the band gap is from the 3p states of the doped S atom with some hybridization of O-2p and Ti-3d states.

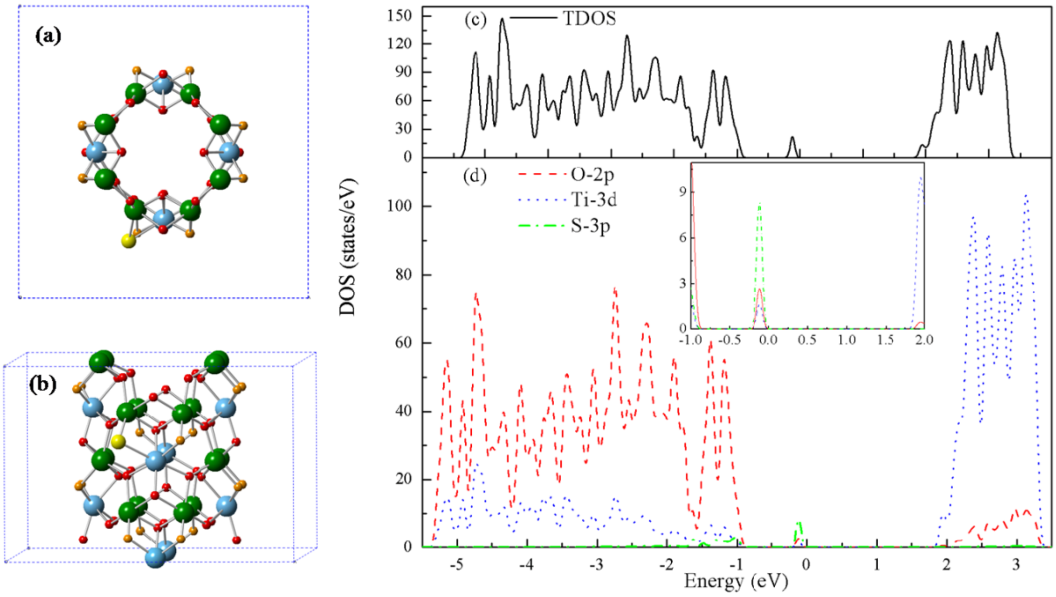

Figure 4.6. The cross-section view (a) and the side view (b) of the most stable structure of S substitution of oxygen in the (6,0) nanotube. The TDOS (c) and PDOS (d) of the S substitution in the (6,0) nanotube. The red dash line represents O-2p states and the blue dot line represents Ti-3d states. The green dash dot line represents S-3p states. The energy zero is set to the top of the occupied states. The detail of the new state is shown in the inset of (d).

The feasibility of the isovalent S substitution in the TiO_2 nanotube has been investigated by calculating the formation energy according to the formula

$$E_{form} = E_{tot}(doped\ \ nanotube) - E_{tot}(clean\ \ nanotube) - \mu_S + \mu_O\ , \qquad (4\text{-}2)$$

where E_{tot} (*doped nanotube*) and E_{tot} (*clean nanotube*) are the total energies of the S-doped and the clean TiO_2 nanotube, respectively. μ_S and μ_O denote the chemical potentials of sulfur and oxygen atom, respectively. The μ_O can be obtained from the ground-state total energy of the O_2 molecule ($\mu_O = \frac{1}{2}\mu_{(O_2)}$), while the μ_S is calculated from the α-S_8. The calculated formation energy for the most stable S-doped TiO_2 nanotube is 2.24 eV per sulfur substitution, making it relatively hard for S to substitute an O atom in the TiO_2 nanotube.

4.3.3.2 The S-adsorption with the (6,0) nanotube

For sulfur adsorption, there are a total of 9 possible highly symmetric adsorption sites both at inner and outer oxygen layers considered in the calculations. However, there are only 6 stable adsorptions left, at which S atom does not relax away from the initial position after the optimization, as shown in Fig. 4.7 (a) and (b). The dashed and solid circles are the top (T) sites for the inner and the outer of the (6,0) nanotube, In-T1, Out-T1, and Out-T2, respectively. The centers of the dashed and solid triangles are the hollow (H) sites for each side of the nanotube, In-H1, In-H2, and Out-H1, respectively. In Table 4.3, the relative energy is

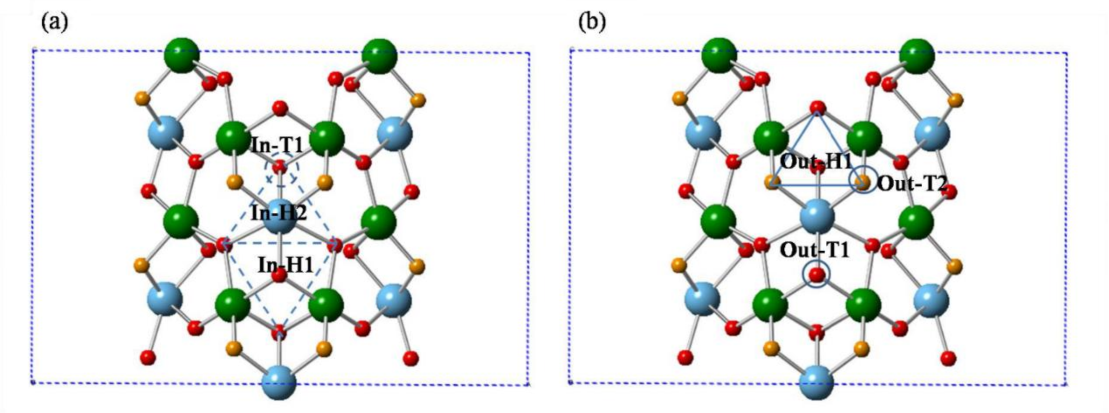

Figure 4.7. The side view of various sites of the sulfur adsorption for the inside (a) and the outside (b) of the (6,0) nanotube with the double c lattice. The bigger green balls are the Ti_{5f} atoms and the bigger blue balls are the Ti_{6f} atoms. The smaller orange balls are the O_{2f} atoms and the smaller red balls are the O_{3f} atoms.

measured from the most stable site, In-H2, shown in Fig. 4.7 (a). As listed in the second row of the Table 4.3, for the most stable adsorption site (In-H2), the first nearest neighbors of the adsorbate sulfur atom are 3 oxygen atoms with an S-O distance of 1.70 Å.

Table 4.3. The relative total energy about the sulfur (S) adsorption with the TiO_2 (6,0) nanotube. The total energy of the most stable adsorption site (In_H2) is set as zero eV.

S-adsorption sites	Relative total energy ΔE_{tot} (eV)
In_H1	0.380
In_H2	0.000
In_T1	0.340
Out_H1	1.835
Out_T1	0.536
Out_T2	1.225

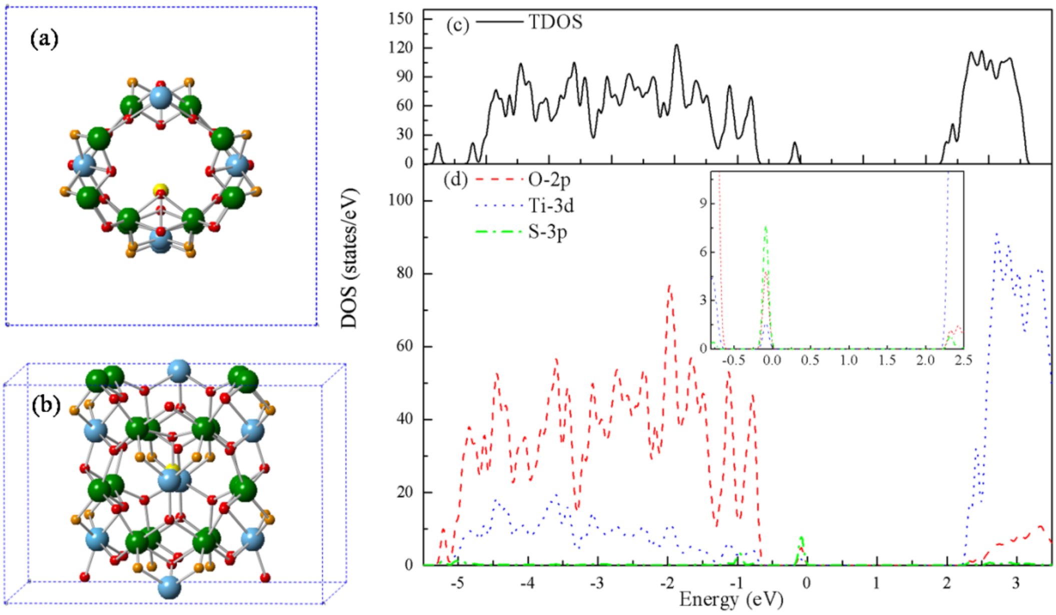

Figure 4.8. The cross-section view (a) and the side view (b) of the most stable structure of S adsorption in the (6,0) nanotube. The TDOS (c) and PDOS (d) of the S adsorption in the (6,0) nanotube. The red dash line represents O-2p states and the blue dot line represents Ti-3d states. The green dash dot line represents S-3p states. The energy zero is set to the top of the occupied states. The detail of the new state is shown in the inset of (d).

The cross-section and side view of the most stable structure for the S-adsorption in the (6,0) nanotube are shown in Fig. 4.8 (a) and (b), respectively. The TDOS and PDOS of the S-adsorption with the (6,0) nanotube are shown in Fig. 4.8 (c) and (d). From the TDOS, it can be estimated that the band gap value is decreased to 2.22 eV. The new occupied states above the original valance bands of the clean (6,0) nanotube are due to the S-adsorption. Fig. 4.8 (d) inset shows that the new states are a hybridization of O-2p, S-3p and Ti-3d orbits.

The absolute band edges of nanotubes cannot be calculated directly with respect to the standard $H_2/H+$ and O_2/H_2O energy level based on the DFT method used. However, the valance band maximum(VBM) and the conduction band minimum (CBM) of the nanotube could be aligned according to the energy of electrons at the core levels of the bulk anatase, such as the 1s state of an oxygen. The VBM for S-adsorption in (6,0) nanotube is 0.97 eV higher than that of the bulk anatase. And the corresponding CBM is 0.26 eV higher than that of the bulk anatase. Therefore, the band gap of the S-adsorped (6,0) nanotube could cover the redox potentials of water splitting, by comparing the band gap position of the bulk anatase with respect to the redox potentials of water splitting [100].

The adsorption energy is calculated as

$$E_{ads} = E_{tot}(\mathrm{S}/nanotube)\text{-}[E_{tot}(nanotube)+E_{tot}(\mathrm{S})], \qquad (4\text{-}3)$$

where $E_{tot}(\mathrm{S}/nanotube)$ is the total energy of the nanotube with the adsorbate sulfur atom on it, $E_{tot}(nanotube)$ is the total energy of the clean nanotube, and $E_{tot}(\mathrm{S})$ represents the total energy of an isolated sulfur atom. By this definition, the more negative the E_{ads} is, the stronger the adsorption becomes. The calculated adsorption energy of the most stable adsorption site is -3.44 eV. This is definitely a chemisorption.

In conclusion, the TiO_2 single-walled have been investigated by the first-principles calculation with the DFT + U approach. The nanotubes constructed by rolling along the (n,0) and (n,n) directions with sizes from n=6 up to n=20 have been studied. The geometry of each nanotube has been fully optimized. The strain energies decrease monotonically with increasing n, except for the (6,0) nanotube. The band gaps of the nanotubes increase monotonically with n, approaching the value of the nanosheet (3.53 eV). The (6,0) nanotube has a structural reconstruction with lowest band gap of ~2.85 eV after relaxation. For sulfur doping, with this reconstructed (6,0) nanotube, sulfur atom at the inner surface of the (6,0) nanotube is preferred. The adsorption energy is calculated as -3.44 eV. This is definitely a chemisorptions.

Chapter 5

TiO_2 double-walled nanotubes

5.1 Introduction

With the rapid development of Nanoscience and Nanotechnology, multiple nanocomposites, nanotube (NT), nanoribbon, nanowire, and nanohorn et al, have drawn lots of attention. Nanotube with the increasing interest, as one of the important nanoscale material members, is kind of a nanometer-scale cylindrical structure. For all the nanotubes with different materials, the most familiar nanotube is the carbon nanotube. As the first observation by Iijima [101] in 1991, the carbon nanotubes (CNTs) have been the focus of more considerable experimental and theoretical research. Numerous investigations about the different kinds of the properties and even the possible applications, from the single-walled (SW) CNTs to double-walled (DW) CNTs and then to multi-wall (MW) CNTs, have been carried out [102, 103]. For the electronic-structure calculations of the double-walled carbon nanotubes [104], the semiconducting energy bands become metallic due to the band edge shift. And the band edge shift is induced by the curvature of the inner tube. Although the more explored nanotube is the carbon nanotube, the nanotubes for other chemical elements or compounds are also attracted by the material scientists. As a graphite-like layered structure with non-carbon material, BN nanotubes have generated lots of interest and studies [105, 106], since BNNTs were predicted by Rubio et al [107, 108] and also synthesized a year later [109]. And other material nanotubes for SiC, Si, and XS_2 (X= Sn, Ti, Zr) have also been investigated experimentally or theoretically [110-113].

As known, TiO_2, as one member of the wide band gap semiconductors, has been extensively studied for photocatalysis, solar cell, lithium batteries, and sensors, due to its robustness, nontoxicity and vast reserves in nature. In recent years, the TiO_2 nanotubes have been discovered by different research groups. The structural and electronic properties of the TiO_2 SWNTs have been analysed theoretically [114, 115]. The different synthetic methods of the TiO_2 nanotubes have also been shown and discussed [116]. It also presents the properties of the TiO_2 nanotubes with different doping chemical elements. On the other hand, compared with the TiO_2 SWNTs, the TiO_2 DWNTs with a large interfacial area are better for the application in photocatalysis [117-119], solar cell [120], and batteries [121]. Moreover, the TiO_2 DWNTs with nitrogen doped experimentally has been prepared [122] and it shows a high water splitting performance, which mainly ascribes to the larger surface areas and expended optical absorption to visible light region. And the TiO_2 DWNTs with the metal decoration, Ag, has also been developed [123] and it also shows an enhanced photocatalytic activity. Although some experimental studies of the TiO_2 DWNTs have been accomplished, there is very little theoretical study about the TiO_2 DWNTs and there is also a lack of comparison with the SWNT base on the density functional theory.

Theoretically, the TiO_2 DWNTs could be built as the combination of the two coaxial SWNTs. So the TiO_2 DWNTs could be studied based on our SWNT work in Chapter 4. The computational details is same as section 4.2 in Chapter 4. In the present work, the structural and electronic properties of DWNTs have been investigated by the first-principles calculations. The binding energies of various TiO_2 DWNTS have been calculated and discussed. And the electronic properties and effective masses are followed for selected TiO_2 DWNTs. These results could make a better understanding of the TiO_2 DWNTs.

5.2 Results and discussions

5.2.1 Structural properties of TiO_2 DWNTs

A TiO_2 DWNT is constructed by two coaxial SWNTs with different diameters. If the SWNT components of the coaxial DWNT have the same chirality types, they would have the equal translational periods, and the DWNT will have the same value of the translational period with the components. In the present work, for simplicity, the coaxial DWNTs with two chiralities, armchair (ac-) $(n_1,n_1)@(n_2,n_2)$ and zigzag (zz-) $(n_1,0)@(n_2,0)$, are considered. For example, the cross-sections of the TiO_2 ac-DWNT and zz-DWNT are shown in Fig.5.1 (a) and (b), respectively. In our previous studies of TiO_2 SWNTs [115], the distance from the axis of the tube to a Ti atom on the tube is set as the radius of the nanotube. For the discussion of the TiO_2 DWNTs, the difference between the average radius of the outer tube and the inner tube is defined as the interwall distance shown in Fig. 5.1 (a).

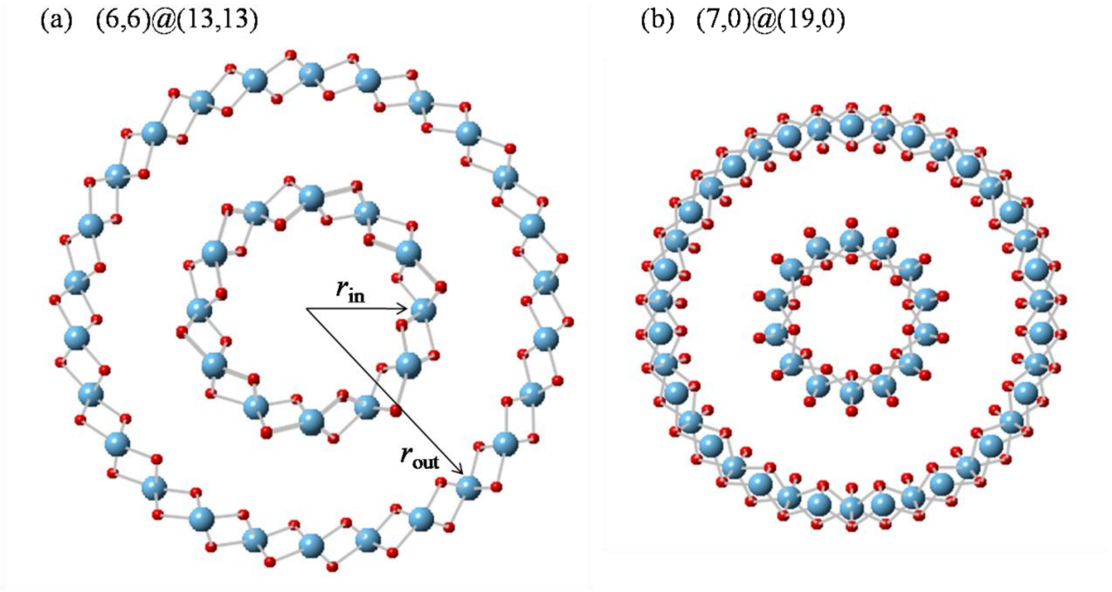

Figure 5.1. (a) The cross-section of TiO_2 DWNT with the armchair chirality indices (6,6)@(13,13). (b) The cross-section of TiO_2 DWNT with the zigzag chirality indices (7,0)@(19,0). The bigger blue balls are the Ti atoms and the smaller red balls are the O atoms.

First, the stability and the preferable interwall spacing of the TiO_2 DWNTs have been explored. As considered the expense of calculation, for the armchair chirality, the two sets of (6,6)@(n,n) and (8,8)@(n,n) DWNTs are chosen for calculation, which the (6,6) and (8,8) are supposed as the inner shell, respectively. Similarly, for the zigzag chirality, the special reconstructed (6,0)@(n,0) and the normal (7,0)@(n,0) DWNTs are being studied. The relative stability of the DWNTs can be calculated by the so-called binding energy E_{bind}. The binding energy E_{bind} between the two constituent shells of the DWNT has been defined as

$$E_{\mathrm{bind}} = E_{\mathrm{tot}}(\mathrm{NT}_{\mathrm{in}}@\mathrm{NT}_{\mathrm{out}}) - E_{\mathrm{tot}}(\mathrm{NT}_{\mathrm{in}}) - E_{\mathrm{tot}}(\mathrm{NT}_{\mathrm{out}}), \qquad (5\text{-}1)$$

where E_{tot}'s are the calculated total energies of the DWNT and its constituent SWNTs after the atomic optimization. To investigate the dependence of the DWNT stability on the interwall distance, a set of ac- and zz-DWNTs with the various radial outer-shell components have been constructed and studied. For the (6,6)@(n,n) and (7,0)@(n,0) DWNTs, the dependence of the binding energy E_{bind} on the interwall distance between the inner and outer SWNT are shown in Fig. 5.2. For the TiO_2 ac-DWNTs, the minima of E_{bind} corresponding to the (6,6)@(13,13) DWNT is around -0.10 eV with the most favorable distance of 5.8-5.9Å, which is as the same as that of the (8,8)@(15,15) DWNT. For the TiO_2 zz-DWNTs, the minima of E_{bind} with the (7,0)@(19,0) DWNT is around -0.14 eV with the distance of 5.4 to 5.6 Å, which is also same with the reconstructed (6,0)@(18,0) DWNT. It can be seen that the binding energy of the TiO_2 zz-DWNTs is a little bit smaller than that of the ac-DWNTs. It means that the configurations of the TiO_2 DWNTs with the zz-chirality are energetically a little more favorable than that with the ac-chirality, which is in agreement with the previous study [124]. And for the most favorable interwall distances of these two chiralities of the DWNTs, the present calculated distances (5.4-5.9 Å) are larger than that observed before [124].

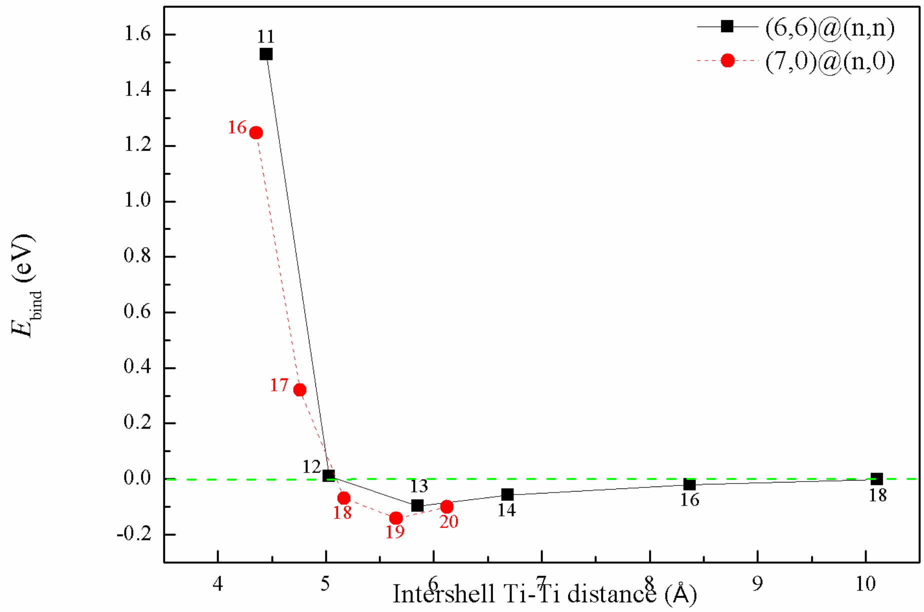

Figure 5.2. The binding energies E_{bind} versus the distance between the shells of the DWNTs with the armchair and zigzag chiralities. The black squares represent the TiO_2 ac-DWNTs (6,6)@(n,n) with n= 11, 12, 13, 14, 16, 18. The red circles represent the TiO_2 zz-DWNTs (7,0)@(n,0) with n= 16, 17, 18, 19, 20.

To investigate the influence of the stacking direction on the stability of DWNTs with the two chiralities, the most stable configurations of the above DWNTs, (6,6)@(13,13) and (7,0)@(19,0), have been studied. There are two parameters to determine the rotation around z axis and the translation along z axis of the inner shell relative to the outer shell, the relative angle $\Delta\varphi$ and the relative shift length Δc, respectively. The z-axis direction is parallel to the translational period direction. The relative binding energy is defined as

$$\Delta E_{bind} = E_{bind}(\text{with } \Delta\varphi \text{ or } \Delta c) - E_{bind}(\Delta\varphi=0 \text{ and } \Delta c=0), \qquad (5\text{-}2)$$

where E_{bind}(with $\Delta\varphi$ or Δc) is the binding energy of the DWNT with the corresponding configuration change of the inner tube and $E_{bind}(\Delta\varphi=0$ and $\Delta c=0)$ is the binding energy of the DWNT without any relative structure change. The relative binding energy function dependent on Δφ and Δc has been shown in the Fig. 5.3 (a) and (b), respectively. In the Fig. 5.3 (a), it shows that for both the two types of DWNTs, the relative binding energy varies within a tiny range from -0.01 eV to 0.01 eV. In Fig. 5.3 (b), the relative binding energy of the TiO_2 ac-DWNT (6,6)@(13,13) has no obvious change with any relative shift. However, the relative binding energy of the TiO_2 zz-DWNT (7,0)@(19,0) exhibits a noticeable change, when the relative shift is about one third of the translational period length, 1/3*c. And the TiO_2 zz-DWNT (7,0)@(19,0) with the 1/3*c shift has the minima value of the binding energy. Therefore, the relative shift along the z-axis direction depends on the tube chirality. So in the configuration studies, the most stable TiO_2 DWNTs are the ac-(6,6)@(13,13) with Δφ=0 and Δc=0 and the zz-(7,0)@(19,0) with Δφ=0 and Δc=1/3*c, respectively.

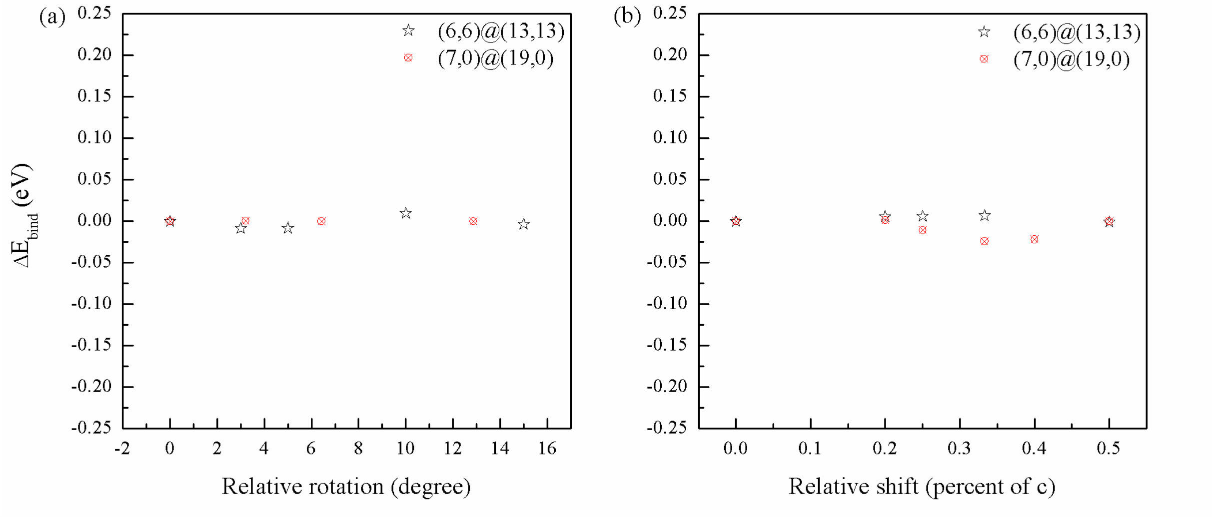

Figure 5.3. The relative binding energies varying with the relative rotation angle (a) and relative shift distance (b) between the inner and outer tubes for the (6,6)@(13,13) and (7,0)@(19,0) DWNTs. The black stars represent the (6,6)@(13,13) DWNT and the red circles represent the (7,0)@(19,0) DWNT.

5.2.2 Electronic properties of TiO_2 DWNTs

To study the electronic properties of the DWNTs, the electronic density of states (DOS) of the DWNTs have been calculated. The DOS of some DWNTs together with the SWNTs is selected in Fig. 5.4. For both two chiralities, the band gap values of the TiO_2 DWNTs are much smaller than that of the SWNTs. For the TiO_2 (6,6)@(13,13) DWNT, the band gap value is reduced to 2.20 eV after the optimization. And for the TiO_2 (7,0)@(19,0) DWNT, the band gap value is reduced to 1.74 eV. They are both reduced in the visible light region. And from Fig. 5.4 (a) and (b), the energy band gap values of the TiO_2 zz-DWNTs are smaller than that of the ac-DWNTs. From the shape of the valance bands and conduction bands, it could be found that the maximum of the valence band (VBM) of the DWNTs is primarily O-2p states, while the minimum of the conduction band (CBM) is dominated by Ti-3d states. From the studies of the DOS of the DWNTs with the same chirality, the band gap value is increased slightly with the increase of the radius of the out shell. However, the band gap value shows evident increment with the increasing radius of the inner shell. And it could speculate that when the radius of the inner tube becomes large enough, the shift-up valence bands would disappear. So it could be found that the appearance of the decreased band gap energy is due to the shift-up states at the valence band edge. The similar phenomenon was also found in the earlier studies of the carbon DWNTs [104]. The main factor of the shift-up valence bands will be discussed in the following part.

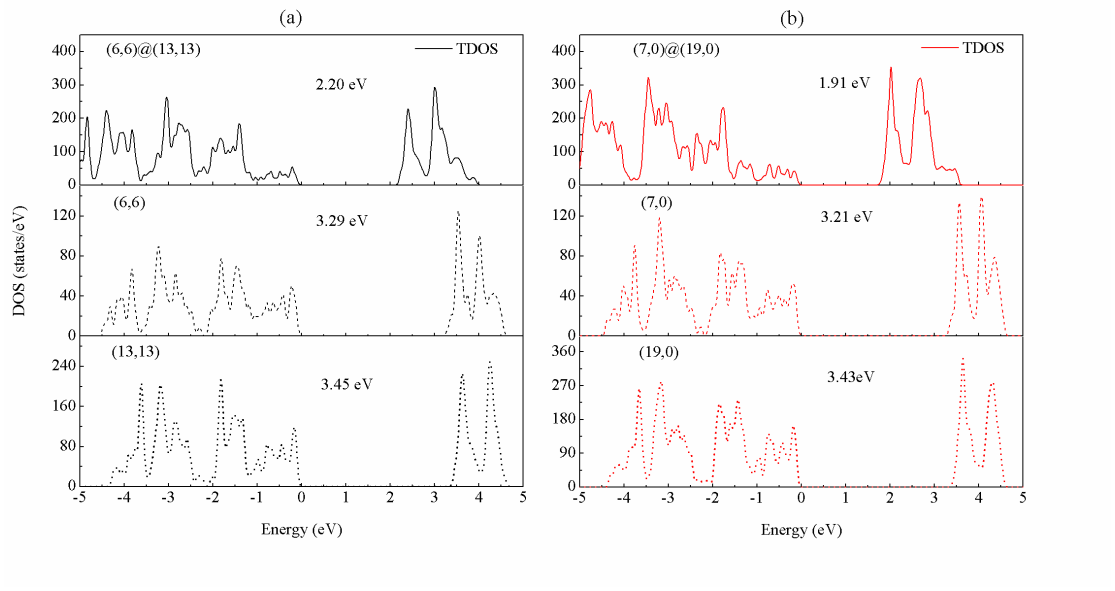

Figure 5.4. The total density of states (TDOS) of the TiO_2 ac-NTs (a) and zz-NTs (b). The black solid line represents the (6,6)@(13,13) DWNT. The black dash line represents the (6,6) SWNT. The black short dash line represents the (13,13) SWNT. The red solid line represents the (7,0)@(19,0) DWNT. The red dash line represents the (7,0) SWNT. The red short dash line represents the (19,0) SWNT. The zero energy is the valence band maximum of each TiO_2 tube.

In order to investigate the band gap reduction in the TiO_2 DWNTs with the relation of inter-wall interaction, one structural model is built, as shown in Fig. 5.5 (a). Since a nanotube would infinitely approach to the nanosheet when its radius continuously increased, the outer shell with the largest radius is supposed to be the HexABC sheet while the inner shell is still kept unchanged as a SWNT. In this model, there are two factors being considered, the intershell Ti-Ti distance and the inner shell radius. The DOS is calculated with respect to various values of the intershell Ti-Ti distance. The intershell Ti-Ti distance values are chosen as 5 Å, 8 Å, and 16 Å respectively, while the inner shell is kept as a (6,6) SWNT. In Fig. 5.5 (c), it could be easily found that the band gap energy varies within 0.01 eV. Then the band gap values of the models are almost independent on the intershell distance. In addition, the DOS relative to varieties of the inner tube radii is studied. The inner tubes are (6,6), (8,8) and (12,12) SWNT with the same intershell Ti-Ti distance of 8 Å. In Fig. 5.5 (d), the band gap values of the models with the three selected inner shells are different as 2.52 eV, 2.77 eV and 3.00 eV. It shows that the band gap energy is mainly dependent on the inner wall radius. The band gap reduction is caused by the shift-up of valence band maximum (VBM) of the inner wall. With the increase of the inner wall radius, the shift-up of VBM would disappear. In other words, the band gap of a DWNT would be increased with the increase of the inner wall radius. Although the DOS reported in Fig. 5.5 (c) and (d) is just about the armchair chirality, the trend is the same for the model of the zigzag chirality. Moreover, deep core levels of Ti atoms from both HexABC sheet and the SWNT are compared. Since both Ti atoms have the same coordination number, i.e. 6 O's, any shift of the levels should be caused by the curvature of the tubes. The energy difference ΔE of the core Ti-1s state between the quasi outer wall, i.e. HexABC sheet, and the inner wall as a function of the curvature, the inverse of the inner shell radius 1/R, is shown in Fig. 5.5 (b). The ΔE of the Ti-1s state leads a roughly linear relation with the curvature 1/R. The shift-up of the valence bands of the inner wall causes the decreasing band gap of the model and hence the DWNTs. The band gap shrinking induced by the curvature of the inner tube itself is also found with the carbon DWNT [104], in which the carbon DWNTs were studied and the curvature of the inner tube was found to cause the metallization in the carbon DWNTs.

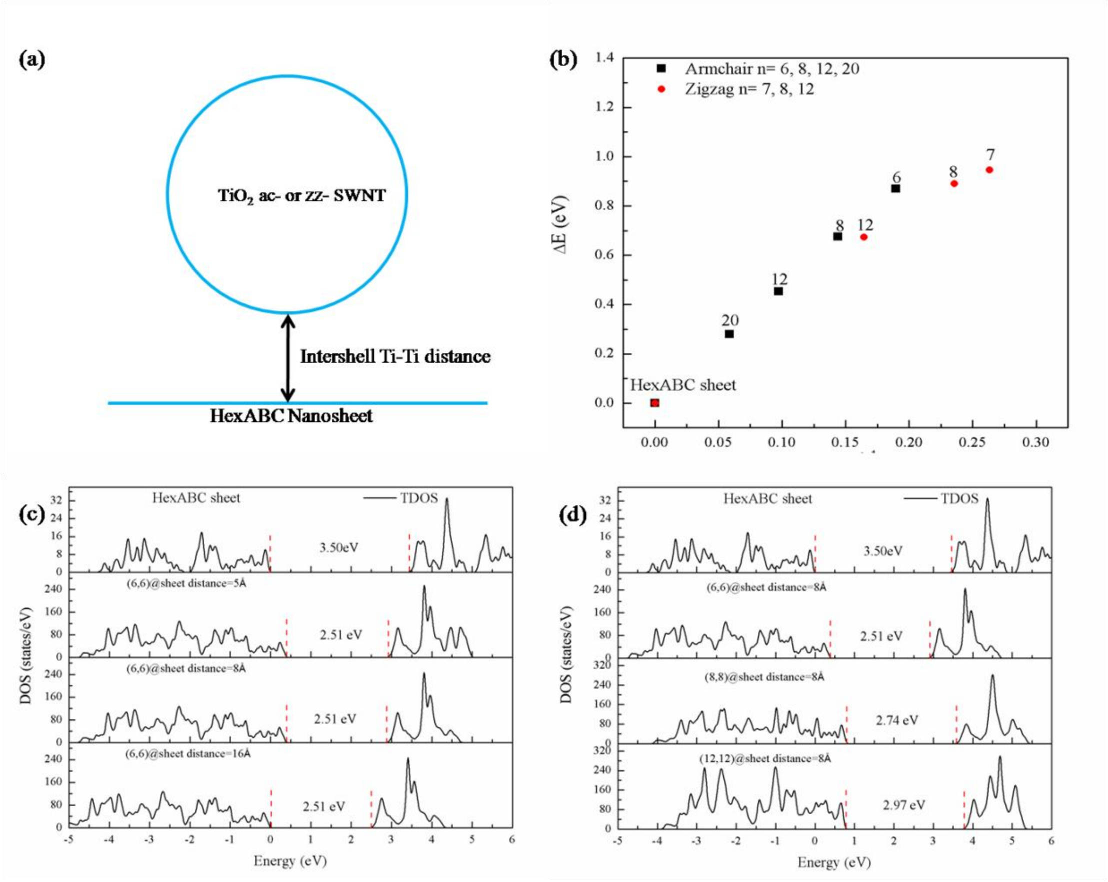

Figure 5.5. (a) The structural model supposed as the combination of a TiO_2 SWNT as the inner tube and a TiO_2 HexABC nanosheet as the outer tube. (b) The energy difference of the Ti-1s states between the inner SWNT and the outer HexABC sheet with respect to the curvature of the inner SWNT. The zero energy is the two-layer HexABC sheet. (c) The DOS of the (6,6)@sheet with the different intershell distance, d=5 Å, 8 Å, and 16Å. (d) The DOS of the (n,n)@sheet with n= 6, 8, 12. The zero energy is the valence band maximum of the TiO_2 HexABC sheet.

To have a better understanding of the band gap reduction of the TiO_2 DWNTs, the band structures and projected DOS of the selected ac- and zz- NTs are shown in Fig. 5.6. From the band structures, the ac-NT has an indirect band gap, while the zz-NT has a direct band gap. For the ac-NTs, the VBM is located at around the Z point and the CBM is located at the Γ point. For the zz-NTs, the VBM and CBM are both at the Γ point. The DOS of the DWNTs has been projected on individual atoms and then regrouped by their constituent SWNTs. It clearly shows that the states of the inner tube for both chiralities shift up from their corresponding SWNT states, causing the reduction of the band gap. This is similar to the case of the Type II band alignment in the semiconducting heterojunctions.

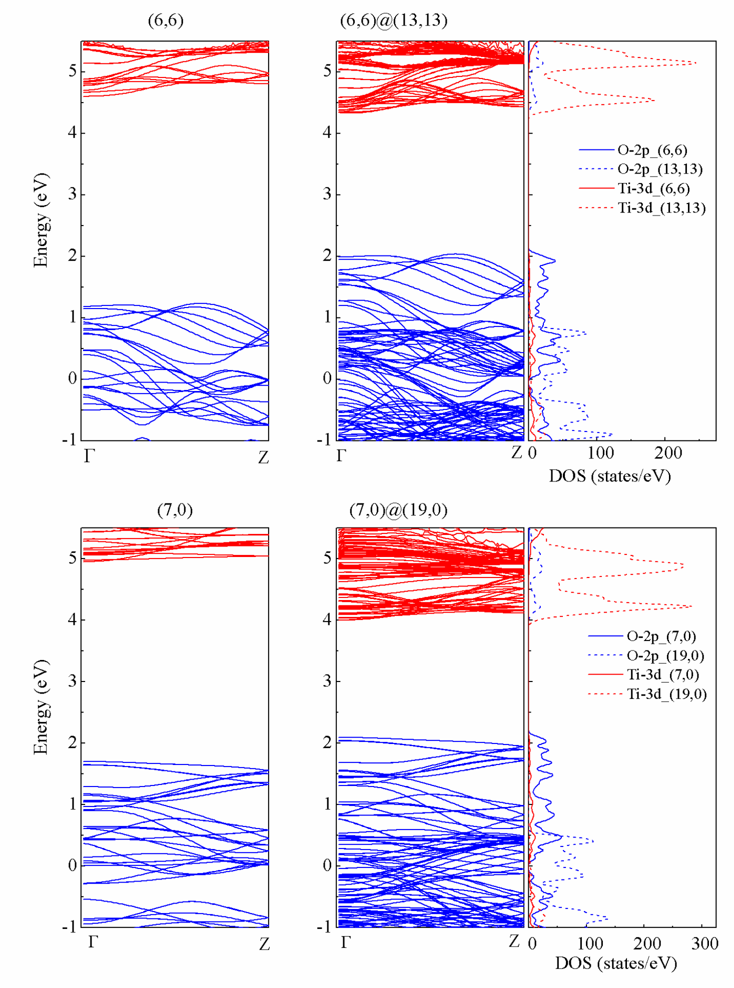

Figure 5.6. The band structures and the partial DOS of the TiO_2 nanotubes. The blue lines represent the valence bands and the red llines represent the conduction bands for the band structures. The blue and red solid lines represent the electronic states of the inner tube. The blue and red dash lines represent the electronic states of the outer tube. The zero energy is the valence band maximum of the TiO_2 HexABC sheet.

The average radii, as indicated in Fig. 5.1(a), and the effective masses of the TiO_2 SWNTs and DWNTs after the structural optimization are included in Table 5.1. The values indicates that the radii of the inner components do not change compared to that of the SWNTs. The effective mass of the electrons and holes are stated in units of the rest mass of a free electron, m_0. For the TiO_2 ac-DWNTs, the effective mass of the hole, m_h*, keeps almost the same with that of the ac-SWNT. And for the zz-DWNTs, m_h* becomes smaller than that of the zz-SWNT.

For the TiO_2 ac-DWNTs, the effective mass of the electron, m_e*, becomes a slightly smaller than that of the ac-SWNT, while on the contrary, the m_e* become a slightly larger than that of the zz-DWNTs. Comparing the effective masses of the ac- and zz- DWNTs, both the m_h* and the m_e* of the ac-DWNTs are much smaller than those of the zz-DWNTs.

Table 5.1. The radii, the energy band gap and the effective mass of the TiO_2 nanotubes. R_{in} and R_{out} mean the radius of the inner tube and outer tube, respectively. m_e* and m_h* are the effective mass of the electron and the hole, respectively. m_0 is the mass of one electron (9.11×10^{-31} kg).

Tubes	R_{in} (Å)	R_{out} (Å)	E_{gap} (eV)	m_e*	m_h*
(6,6)	5.27	--	3.29	$2.38m_0$	$0.52m_0$
(8,8)	6.93	--	3.40	$1.51m_0$	$0.53m_0$
(6,6)@(12,12)	5.25	10.28	2.14	$1.35m_0$	$0.54m_0$
(6,6)@(13,13)	5.27	11.12	2.20	$0.96m_0$	$0.52m_0$
(6,6)@(15,15)	5.27	12.83	2.22	$0.97m_0$	$0.52m_0$
(6,6)@(18,18)	5.27	15.38	2.31	$0.89m_0$	$0.52m_0$
(8,8)@(15,15)	6.84	12.82	2.43	$0.89m_0$	$0.52m_0$
(8,8)@(18,18)	6.89	15.38	2.45	$0.89m_0$	$0.52m_0$
(7,0)	3.80	--	3.21	$1.68m_0$	$7.44m_0$
(7,0)@(18,0)	3.79	8.97	1.86	$2.31m_0$	$6.41m_0$
(7,0)@(19,0)	3.80	9.45	1.91	$2.20m_0$	$6.67m_0$
(7,0)@(20,0)	3.80	9.92	1.93	$2.35m_0$	$6.78m_0$

For photocatalysic materials, a key point is whether the band edges could cover the potential energy of the redox reactions. Since the periodic boundary condition is used for modeling a large system, such as a DWNT, there is no real infinity in the system studied. It means that the absolute zero energy point is not well defined. Therefore, the absolute band edges of the nanotubes studied in present work cannot be calculated directly with respect to the standard H_2/H+ and O_2/H_2O energy level based on the DFT method used. But we can indirectly estimate the position of the band edges using the well-known bulk TiO_2 band egge positions relative to the redox reaction levels. For the bulk and the two-dimensional HexABC sheet, the band edge position could be aligned according to the energy of electrons at the core levels, such as the 1s state of an Ti atom, since the coordination number of Ti atoms in both systems is the same. And for the two-dimensional and one-dimensional structures, the band edge position could be aligned according to choosing a relative vacuum point. The band edges of the TiO_2 HexABC sheet and selected TiO_2 nanotubes relative to the redox potentials of water splitting are shown in Fig. 5.7. It shows that all the nanotubes could cover the redox potentials of water splitting. Although the band gap energies for the TiO_2 DWNTs, are decreased into the visible light energy range compared with the TiO_2 SWNTs, it is the consequence of the band misalignment of the constituent SWNTs due to the curvature difference. However, the misalignment of the VBM and CBM may help the separation of electrons and holes, reducing the recombination of the pairs.

To sum up, the TiO_2 DWNTs of the armchair and the zigzag chiralities could be built by two coaxial single-walled nanotubes with different diameters. The binding energies of the TiO_2 DWNTs with respect to the interwall distance for the two different chiralities have been calculated. The TiO_2 ac-DWNTs and the zz-DWNTs with the optimal interwall distance are (6,6)@(13,13) with about 5.85 Å and (7,0)@(19,0) with about 5.50 Å, respectively. Then the electronic properties of the TiO_2 DWNTs have been investigated. The band gap energies of the TiO_2 DWNTs are significantly smaller than that of the SWNTs, caused by the band shift on constituent SWNTs. And the band shift is mainly dependent on the curvature of a tube. As results, the band edge alignment of the TiO_2 DWNTs forms a type II band alignment, the staggered gap. And the band gap of the NTs could cover the redox potentials of water splitting, by comparing the band gap position of the bulk anatase with respect to the redox potentials of water splitting.

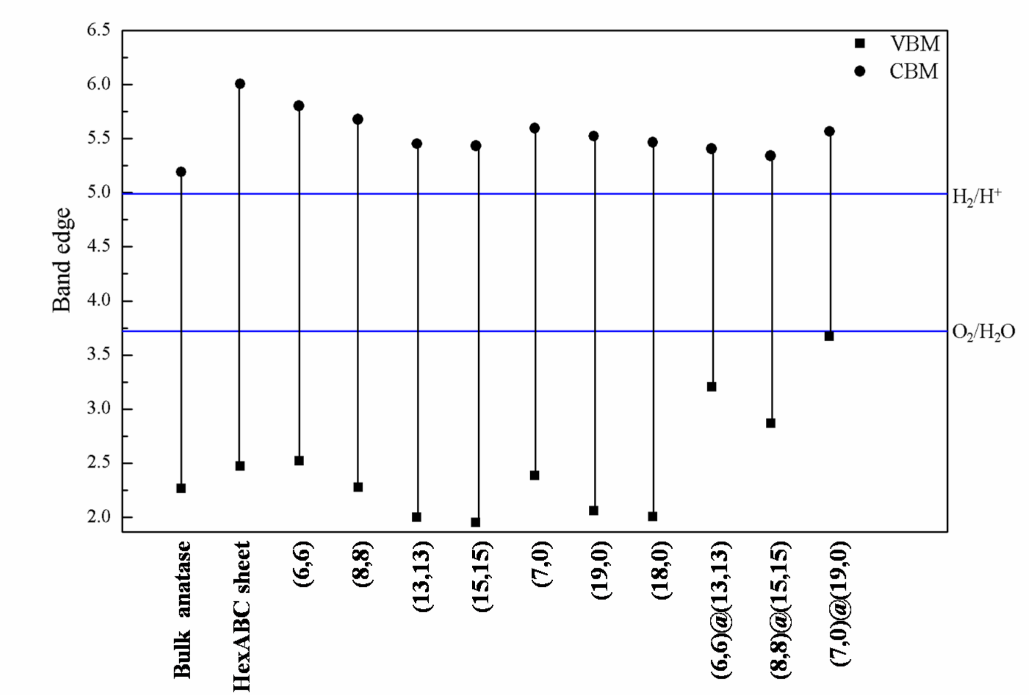

Figure 5.7. The band edge alignment according to the Ti_1s state energy and the vacuum energy. The two blue horizontal lines are the energies.of the redox potentials.

Chapter 6

Conclusions

In summary, we have applied the first-principles method to study the selected semiconducting transition metal oxides. We have studied the stability of the clean hematite α-Fe_2O_3 (0001) film built of 12 atomic layers with two different types of termination by DFT + U method. The film terminated by Fe atoms on both sides with the AFM arrangement is the most stable one. For a sulfur adsorption on the suface of this model, various sites have been examined. It is found that the S adatom prefers to bond with the three O atoms on the second layer of the surface, in the centre of the equilateral triangle formed by the three O atoms. Comparing with the DOS of the clean film, there are two gap states in the band gap due to the adsorption, in addition to the original surface states. The S adatom acts as a cation here, and has no direct contribution to the gap states of the film electronic structure. Meanwhile, the S atom substitution of the first layer O atom is energetically 0.56 eV lower than that of the substitution of the second layer O atom. From the study of the electronic properties of the S-doping in the film, it shows that the band gap is reduced to ~1.26 eV from ~1.43 eV of the clean film, similar to the S-doping in bulk Fe_2O_3. The results of both the adsorption and the substitution by S atom at the α-Fe_2O_3 (0001) surface suggest that S atom prefers to stay at the surface and it could be difficult to be doped into the material and modify the band gap of α-Fe_2O_3 as previous expected. This excludes the possibility of tuning the band gap of α-Fe_2O_3 through the sulfurization of the oxide surfaces, followed by thermal diffusions. Therefore, the doping of S in α-Fe_2O_3 should be investigated by alternative ways, such as ion implementation followed by thermal annealing.

The TiO_2 single-walled and double-walled nanotubes have been investigated by the first-principles calculation with the DFT + U approach. The most stable single layer TiO_2 nanosheet has been identified as TiO_2 HexABC structure. The corresponding single-wall nanotubes can be constructed by rolling along the (n,0) and (n,n) directions. The nanotubes with sizes from n=6 up to n=20 have been studied. The geometry of each nanotube has been fully optimized. The strain energies decrease monotonically with increasing n, except for the (6,0) nanotube. The band gaps of the nanotubes increase monotonically with n, approaching the value of the nanosheet (3.53 eV). They are higher than the band gap values of the bulk TiO_2 in general. However, the (6,0) nanotube has a substantial structural relaxation. It has the lowest band gap of ~2.85 eV, falling between the calculated values of the TiO_2, bulk rutile and anatase. Therefore, the most stable low-dimensional nanotube structure, constructed by rolling the TiO_2 HexABC nanosheet, does not cause the reduction of the band gaps as expected originally. However, the isovalent impurities, such as sulfur, could be introduced into the low-dimensional structures more easily than that of the bulk materials. The (6,0) nanotube with the lowest band gap is picked to investigate S substitution of oxygen and S adsorption on it. Indeed, the band gap was further reduced to 1.84 eV for S substitution and 2.22 eV for S adsorption, respectively. Energetically, S adsorption at the inner surface of the (6,0) nanotube is preferred. It shows that the promising sulfurization of TiO_2 nanotubes with a reduced band gap could make it visible light sensitive.

The TiO_2 DWNTs of the armchair and the zigzag chiralities could be built by two coaxial single-walled nanotubes with different diameters. The structural properties of the TiO_2

DWNTs have been studied. The binding energies of the TiO_2 DWNTs with respect to the interwall distance for the two different chiralities have been calculated. The TiO_2 ac-DWNTs and the zz-DWNTs with the optimal interwall distance are (6,6)@(13,13) with about 5.85 Å and (7,0)@(19,0) with about 5.50 Å, respectively. The binding energy of the (7,0)@(19,0) DWNT is 0.04 eV a bit of smaller than that of the (6,6)@(13,13) DWNT. It shows that the TiO_2 zz-DWNT is energetically more favorable than that of the ac-DWNT. Then the electronic properties of the TiO_2 DWNTs have been investigated. And the band gap energies of the TiO_2 DWNTs are significantly smaller than that of the SWNTs. It is found that this is purely caused by the band shift on constituent SWNTs. And the band shift is mainly dependent on the curvature of a tube. As results, the band edge alignment of the TiO_2 DWNTs forms a type II band alignment, the staggered gap. It may reduce the recombination of electron-hole pairs. And the band gap of the NTs could cover the redox potentials of water splitting, by comparing the band gap position of the bulk anatase with respect to the redox potentials of water splitting.

REFERENCES

[1] https://www.iea.org/weo/

[2] Bhubaneswari Parida, S. Iniyan, and Ranko Goic Renewable and Sustainable Energy Reviews 15 2011 1625–1636.

[3] Fujishima A. and Honda K. Nature 1972, 238, 37-38.

[4] S. Girish Kumar and L. Gomathi Devi J. Phys. Chem. A 2011, 115, 13211–13241.

[5] Dmitry V. Bavykin, Jens M. Friedrich, and Frank C. Walsh Adv. Mater. 2006, 18, 2807–2824.

[6] Jian Tian, Zhenhuan Zhao, Anil Kumar,b Robert I. Boughton, and Hong Liu *Chem. Soc. Rev.,* 2014, 43, 6920—6937.

[7] M. Born and R. Oppenheimer, Annalen der Physik 1927 389, Issue 20, pages 457–484.

[8] D. R. Hartree. Theory and Methods, Mathematical Proceedings of the Cambridge Philosophical Society 1928, 24, 89-110.

[9] V. Fock. Zeitschrift für Physik 1930, 61, 126-148.

[10] Fermi E. Rend Accad Naz Lincei. 1927, 32: 602-607.

[11] Thomas LH. Proceedings of the Royal Society of London Series A. 1927, 114 (768): 561-76.

[12] P. Hohenberg and W. Kohn. Physical Review 1964 136, B864- B871.

[13] W. Kohn and L. J. Sham. Physical Review 1965 140, A1133-A1138.

[14] Felix Bloch (1928). Magazine for physics July 1929, Volume 52, Issue 7-8 , pp 555-600

[15] J. C. Slater, Koster GF. Simplified LCAO method for the periodic potential problem Physical Review. 1954, 94(6): 1498.

[16] Charles Kittel, Introduction to Solid State Physics, University ofCalifornia, Berkeley, 1953

[17] Hedin, L., B.I. Lundqvist 1971 *Journal of Physics C*, 4, 2064.

[18] Von Barth, U., L. Hedin 1972 *Journal of Physics* C: *Solid State Physics* 5, 1629.

[19] J. P. Perdew. *Phys. Rev. Lett.*, 1985 55:1665.

[20] J. Heyd, G. E. Scuseria, and M. Ernzerhof, 2003 J. Chem. Phys. 118, 8207.

[21] A. V. Krukau , O. A. Vydrov, A. F. Izmaylov, and G. E. Scuseria, J. Chem. Phys. 2006 125, 224106.

[22] Hedin L. New method for calculating the one-particle Green's function with application to the electron-gas problem. Physical Review. 1965, 139(3A): A796-A823.

[23] Vanderbilt D. Soft self-consistent pseudopotentials in a generalized eigenvalue formalism[J]. Physical Review B. 1990, 41(11): 7892-5.

[24] G. Kresse, Joubert D. From ultrasoft pseudopotentials to the projector augmented-wave method[J]. Physical Review B. 1999, 59(3): 1758-75.

[25] Teja A.S., Koh, P.Y., Prog. Cryst. Growth Charact. Mater. 2009, 55, 22-45.

[26] Mahmoudi M., Simchi I., Imani M., J. Iran. Chem. Soc., 2010, 7, S1-S27.

[27] Wang G., Liu T., Luo Y., Zhao Y., Ren Z., Bai, J., Wang H., J. Alloys Compd., 2011, 509, L216-L220.

[28] Gupta A.K., Gupta M., Biomaterials 2005, 26, 3995-4021.

[29] Larry W. Finger and Robert M. Hazen, J. Appl. Phys., 1980, 51, 5362-5367.

[30] J. Staun Olsen, C. S. G. Cousins, L. Gerward, H. Jhans and B. J. Sheldon, Physica Scripta, 1991, 43, 327-330.

[31] F. J. Morin, Phys. Rev., 1953, 93, 1195-1199.

[32] C. Gieitzer, J. Nowotny and M. Rekas, Appl. Phys. A, 1991, 53, 310-316.

[33] G. Rollmann, A. Rohrbach, P. Entel, J. Hafner, Phys. Rev. B, 2004, 69, 165107.

[34] A. H. Hill, F. Jiao, P. G. Bruce, A. Harrison, W. Kockelmann, and C. Ritter, Chem. Mater., 2008, 20, 4891-4899.

[35] Carlos J Serna, Manuel Ocafia and Juan E Iglesias, J. Phys. C: Solid State Phys., 1987, 20, 473-484.

[36] Tadanori Hashimoto, Tetsuya Yamada, and Toshinobu Yoko, J. Appl. Phys., 1996, 80, 3184-3190.

[37] Kevin Sivula, Florian Le Formal, and Michael Grätzel, ChemSusChem, 2011, 4, 432-449.

[38] Yuzheng Guo, Stewart J Clark, and John Robertson, J. Phys.: Condens. Matter, 2012, 24, 325504.

[39] Alan Kleiman-Shwarsctein, Yong-Sheng Hu, Arnold J. Forman, Galen D. Stucky, and Eric W. McFarland, J. Phys. Chem. C, 2008, 112, 15900-15907.

[40] Ilkay Cesar, Andreas Kay, José A. Gonzalez Martinez, and Michael Grätzel, J. Am. Chem. Soc., 2006, 128, 4582-4583.

[41] Yong-Sheng Hu, Alan Kleiman-Shwarsctein, Arnold J. Forman, Daniel Hazen, Jung-Nam Park, and Eric W. McFarland, Chem. Mater., 2008, 20, 3803-3805.

[42] Omid Zandi, Benjamin M. Klahr and Thomas W. Hamann, Energy Environ. Sci., 2013, 6, 634-642.

[43] Peilin Liao, John A. Keith, and Emily A. Carter, J. Am. Chem. Soc., 2012, 134,

13296-13309.

[44] Nerine J. Cherepy, Dorion B. Liston, Jennifer A. Lovejoy, Hongmei Deng, and Jin Z. Zhang, J. Phys. Chem. B, 1998, 102, 770-776.

[45] Alan Kleiman-Shwarsctein, Muhammad N. Huda, Aron Walsh, Yanfa Yan, Galen D. Stucky, Yong-Sheng Hu, Mowafak M. Al-Jassim, and Eric W. McFarland, Chem. Mater., 2010, 22, 510-517.

[46] T. Droubay, K. M. Rosso, S. M. Heald, D. E. McCready, C. M. Wang, and S. A. Chambers, Phys. Rev. B, 2007, 75, 104412.

[47] X. Y. Meng, G. W. Qin, S. Li, X. H. Wen, Y. P. Ren, W. L. Pei and L. Zuo, Appl. Phys. Lett., 2011, 98, 112104.

[48] Congxin Xia, Yu Jia, Meng Tao, and Qiming Zhang, Physics Letters A, 2013, 377, 1943-1947.

[49] Wolfgang Bergermayer and Hannes Schweiger, Phys. Rev. B, 2004, 69, 195409.

[50] Manh-Thuong Nguyen and Ralph Gebauer, J. Phys. Chem. C, 2014, 118, 8455-8461.

[51] Jiajia Song , Xiaoqi Niu , Lixia Ling , Baojun Wang, Fuel Processing Technology, 2013, 115, 26-33.

[52] Frank J. Berry, Alberto Bohorquez, Colin Greaves, Julia McManus, Elaine A. Moore, Michael Mortimer, J. Solid State Chem., 1998, 140, 428-430.

[53] Adam Kiejna and Tomasz Pabisiak, J. Phys.: Condens. Matter, 2012, 24, 095003.

[54] Kresse G and Hafner J, Phys. Rev. B, 1993, 47, 558.

[55] Kresse G and Furthmüller J, Phys. Rev. B, 1996, 54, 11169.

[56] J.P. Perdew, J.A. Chevary, S.H. Vosko, K.A. Jackson, M.R. Pederson, D.J. Singh, C.

Fiolhais, Phys. Rev. B, 1992, 46, 6671–6687.

[57] Dudarev S L, Botton G A, Savrasov S Y, Humphreys C J and Sutton A P, Phys. Rev. B, 1998, 57,1505.

[58] Graeme Henkelman, Blas P. Uberuaga and Hannes Jónsson, J. Chem. Phys., 2000, 113, 9901.

[59] Hendrik J. Monkhorst and James D. Pack, Phys. Rev. B, 1976, 13, 5188.

[60] Graeme Henkelman, Andri Arnaldsson, and Hannes Jónsson, Computational Materials Science, 2006, 36, 354-360.

[61] Bianchi L. C., Pirola C., Stucchi M., *et al* (2016) Semiconductor Photocatalysis - Materials, Mechanics and Applications 23:635-666

[62] Grätzel M. (2003) Journal of Photochemistry and Photobiology C: Photochemistry Reviews 4:145-153

[63] Bavykin V. D., Lapkin A. A., Plucinski K. P., Friedrich M. J., Walsh C. F. (2005) J. Phys. Chem. B 109:19422-19427

[64] Bamwenda R. G., Tsubota S., Nakamura T., Haruta M. (1995) J Photochem Photobiol A: Chem 89:177-189

[65] Islam M. M, Calatayud M., Pacchioni G. (2011) J Phys Chem C 115:6809-6814

[66] Michael G. (2001). NATURE 414:338-344

[67] Hashimoto K., Irie H., Fujishima A. (2005) Japanese Journal of Applied Physics 44:8269-8285

[68] Carp O., Huisman C. L., Reller A. (2004) Progress in Solid State Chemistry 32:33-177

[69] Dachillf F., Simons Y. P., Roy R. (1968) The American Mineralogist 53:1929-1939

[70] Mo S-D, Ching W. Y. (1995) Phys Rev B 51:13023-13032

[71] Landmann M., Rauls E., Schmidt W. G. (2012) J Phys: Condens Matter 24:195503

[72] Tang H., Lévy F., Berger H., Schmid P. E. (1995) Phys Rev B 52:7771-7774

[73] Amtout A., Leonelli R. (1995) Phys Rev B 51:6842-6851

[74] Jafari T., Moharreri E., Amin A. S., Miao R., Song W., Suib L. S. (2016) Molecules 21: 900

[75] Kumar S. G., Devi G. L. (2011) J Phys Chem A 115:13211-13241

[76] Linsebigler L. A., Lu G., Yates T. J. (1995) Chem Rev 95:735-758

[77] Choi W., Termin A., Hoffmann R M. (1994) J Phys Chem 98:13669-13679

[78] Devi L. G., Kavitha R. (2013) Applied Catalysis B: Environmental 140-141:559-587

[79] Yang Z-Q, Qin L-L, Tian P-W, Zhang Y-X (2014) IPCBEE 78:31-40

[80] Zaleska A. (2008) Recent Patents on Engineering 2:1872-2121

[81] Hattori A., Tokihisa Y., Tada H., Itob S. (2000) Journal of The Electrochemical Society 147:2279-2283

[82] Akpan U. G., Hameed B. H. (2009) Journal of Hazardous Materials 170:520-529

[83] Ugeda M. M., Bradley J. A., Shi S-F *et al* (2014) Nature Materials 13:1091-1095

[84] Wang Q. H, Kalantar-Zadeh K., Kis A., Coleman N. J., Strano S. M. (2012) Nature Nanotechnology 7:699-712

[85] Zhang Y., Tang Z-R, Fu X., Xu Y-J (2011) ACS Nano 5:7426-7435

[86] Barreca D., Carraro G., Comini E., Gasparotto A., Maccato C., Sada C., Sberveglieri G., Tondello E. (2011) J Phys Chem C 115:10510-10517

[87] Gong D., Craig A. G., Oomman K. V. (2001) J Mater Res 16:3331-3334

[88] Lazzeri M., Vittadini A., Selloni A. (2001) Phys Rev B 63:155409

[89] Pascual J., Camassel J., Mathieu H. (1977) Phys Rev Lett 39:1490-1493

[90] Tang H., Berger H., Schmid P. E., Levy F. (1993) Solid State Communications 87:847-850

[91] Heyd J., Scuseria G. E., Ernzerhof M. (2003) J Chem Phys 118:8207-8215

[92] Krukau A. V., Vydrov O. A., Izmaylov A. F., Scuseria G. E. (2006) J Chem Phys 125:224106

[93] Meng Q. Q., Wang J-G, Xie Q., Li X-N. (2010) J Phys Chem C 114:9251-9256

[94] Mowbray D. J., Martinez J. I., Garcıa-Lastra J. M., Thygesen K. S., Jacobsen K. W. (2009) J Phys Chem C 113:12301-12308

[95] Maeda T., Kobayashi Y., and Kishi K. (1999) Surface Science 436: 249-258

[96] Mannig A., Zhao Z., Rosenthal D., Christmann K., Hoster H., Rauscher H., Behm R.J. (2005) Surface Science 576: 29-44

[97] Tao J., Luttrell T., and Batzill M. (2011) Nature Chemistry 3:296-300

[98] Dresselhaus M. S., Dresselhaus G., and Eklund P. C. (1996) (Academic, San Diego)

[99] Blasé X., Rubio A., Louie S. G., and Cohen M. K. (1994) Europhys. Lett. 28:335-340

[100] Ong W. J., Tan L. L., Ng Y. H., Yong S-T, and Chai S-P (2016) *Chem. Rev.* 116: 7159-7329

[101] Sumio lijima (1991) NATURE 354: 56-58.

[102] Cai Shen, Alexandra H. Brozena and YuHuang Wang (2011) Nanoscale 3: 503-518.

[103] Khalid Saeed Ibrahim (2013) Carbon Letters 14: 131-144.

[104] Susumu Okada and Atsushi Oshiyama (2003) Phys Rev Lett 91: 216801.

[105] Saban Kalay, Zehra Yilmaz, Ozlem Sen, Melis Emanet, Emine Kazanc and Mustafa Çulha (2015) Beilstein J. Nanotechnol. 6: 84-102.

[106] Jun Hee Kim, Thang Viet Pham, Jae Hun Hwang, Cheol Sang Kim and Myung Jong Kim (2018) Nano Convergence 5:17.

[107] A. Rubio, J.L. Corkill, and M.L. Cohen (1994) Phys Rev B 49: 5081-5084.

[108] X. Blase, A. Rubio, S.G. Louie, and M.L. Cohen (1994) Europhys Lett 28: 335-340.

[109] Nasreen G. Chopra, R. J. Luyken, K. Cherrey, Vincent H. Crespi, Marvin L. Cohen, Steven G. Louie, and A. Zettl. (1995) Science 269: 966-967.

[110] Madhu Menon (2004) Phys Rev B 69: 115322.

[111] Matheus P Lima (2018) Nanotechnology 29: 075703.

[112] Andrei V. Bandura and Robert A. Evarestov. (2015) Surface Science 641: 6-15.

[113] Andrei V. Bandura and Robert A. Evarestov (2014) Journal of Computational Chemistry 35: 395-405.

[114] Tao He, Mingwen Zhao, Xuejuan Zhang, Hongyu Zhang, Zhenhai Wang, Zexiao Xi, Xiangdong Liu, Shishen Yan, Yueyuan Xia, and Liangmo Mei (2009) J. Phys. Chem. C 113: 13610-13615.

[115] Jiao An, Yuting Peng, and Qiming Zhang (2018) J Mater Sci 53:15530-15540.

[116] Yu Fu and Anchun Mo (2018) Nanoscale Research Letters 13:187.

[117] Kun Liang, Beng Kang Tay, Olga V. Kupreeva, Taisiya I. Orekhovskaya, Sergei K. Lazarouk, and Victor E. Borisenko (2014) ACS Sustainable Chem. Eng. 2: 991-995.

[118] Chaorui Xue, Takashi Narushima, Yohei Ishida, Tomoharu Tokunaga, and Tetsu Yonezawa (2014) ACS Appl. Mater. Interfaces 6: 19924-19932.

[119] Yan Liu, Kangsheng Mu, Gang Yang, Hong Peng, Fei Shen, Lilin Wang, Shihuai Deng, Xiaohong Zhang and Yanzong Zhang (2015) New J. Chem. 39: 3923-3928.

[120] Wei-Chieh Chen, Min-Hsin Yeh, Lu-Yin Lin, R. Vittal, and Kuo-Chuan Ho (2018) ACS Sustainable Chem. Eng. 6: 3907-3915.

[121] Jose R. Gonza lez, Ekaterina Zhecheva, Radostina Stoyanova, Diana Nihtianova, Pavel Markov, Regis Ravelle Chapuis, Ricardo Alcantara, Francisco Nacimiento, Jose L. Tiradoa and Gregorio F. Ortiza (2015) Phys. Chem. Chem. Phys. 17: 4687-4695.

[122] Hongjun Wu and Zhonghai Zhang (2011) International journal of hydrogen energy 36: 13481-13487.

[123] Chao Zhang, Yuming Zhou, Yiwei Zhang, Shuo Zhao, Jiasheng Fang, and Xiaoli Sheng (2017) Appl Organometal Chem. 32: 4160.

[124] R. A. Evarestov,Yu. F. Zhukovskii, A. V. Bandura, S. Piskunov and M.V. Losev (2011) J. Phys. Chem. C 29: 14067-14076.